Chapter 4

Inhomogeneous Big Bang Nucleosynthesis

This chapter deals with work done using a BBN code this author has written for an inhomogeneous model of the universe. The model for the baryon distribution used in this IBBN code is a lattice of spheres whose centers are equally spaced between each other. One sphere is composed of spherical shells that each have their own value of baryon density ρ_b, and the sphere is considered characteristic of this model of the universe. This chapter first reviews the journal articles that discuss scenarios that could plausibly lead to an inhomogeneous baryon distribution like that in this IBBN code. Then the chapter discusses the details of how the IBBN codes of other journal articles work, some details which were use for this author's own code. Then the chapter shows how new parameters such as the size of a region and the contrast between high and low baryon densities alter the final mass fractions from the Texas code's results, for both light isotopes like ^{4}He and the heavier isotopes added to the Texas code in Chapter (2). Finally the chapter discusses how the IBBN code's results change when it's run with the neutrino heating effect turned on.

4.1 Background

Papers such as (Witten, 1984) [42] and (Kurki-Suonio, 1988) [43] were the first articles to describe scenarios in the universe's evolution that lead to the universe having an inhomogeneous baryon distribution by the time when temperature T reaches 100 GK. The most popular scenario was a first-order phase QCD phase transition from a quark-gluon plasma to a hadronic gas, occuring when T is around 2000 GK. Here the universe cools until it reaches a coexistence temperature T_c when quarks start to nucleate and form bubbles of hadronic gas. A first order transition means that the hadronic bubbles release enough latent heat to make up for the heat the quark-gluon plasma loses from the expansion of the universe, and so the universe maintains a temperature T_c for a period of time. The hadronic gas bubbles grow large enough to coelesce, and the regions of quark-gluon plasma become separate bubbles in the hadronic gas. The quark-gluon plasma bubbles all get converted to hadronic gas by the end of the phase transition. But the plasma bubbles tend to have a higher baryon number than the hadronic gas. It has been speculated that the bubbles with higher baryon number will leave clumps of higher baryon density centered at the points where the centers of the bubbles once were [44]. The exact mechanisms by which the phase transition leaves these clumps is poorly understood. Articles such as (Kurki-Suonio, 1988) speculated on several such mechanisms. An alternative theory has baryons forming in an electroweak phase transition that occurs when T is around one million GK. Bubbles of hadronic gas form and rapidly expand, with nucleation occuring most rapidly at the bubble walls. After the phase transition the bubble walls expand only due to the universe's expansion, and expand more slowly than before. The result is a higher baryon density around the bubble walls and a low density within them [45], the opposite distribution of that generated by the QCD phase transition.

The motivation to write inhomogeneous codes in the 1970's and 1980's was to find a model with a baryon density, averaged over all the regions, equal to the critical density ($\Omega_b = 1.0$, $\eta_{10} = 70.0$) that satisfies observational values of the light elements. At $\eta_{10} = 70.0$ ^{4}He is overproduced while deuterium is underproduced. The earliest articles on inhomogeneous codes [46] treated the different density regions as separate standard BBN models. They would run a standard code with a high value of ρ_b, then run it with a low value, and then average the resulting mass fractions from the runs according to how large the high and low density regions were. The high density runs and the low density runs would always start with the same mass fraction ratio $X_{\mathrm{n}}/X_{\mathrm{p}}$ of neutrons to protons. In the late 1980's articles considered the effect of nucleon diffusion on the final results. For instance in the QCD phase transition model and the electroweak phase model neutrons could diffuse from the high density regions to the low, obeying the equation

$$\frac{\partial n_{\mathrm{n}}}{\partial t} = D_n \nabla^2 n_n \tag{4.1}$$

n_{n} is the neutron number density and D_{n} is the diffusion coefficient. In a 1987 article Applegate, Hogan and Scherrer [47] noted that neutrons could diffuse into the low density regions via scattering off of electrons and protons, and that the low density regions could be neutron rich by the time nucleosynthesis begins. On the other hand protons would be scattered off of electrons more than the neutrons because the protons have a charge. The protons would diffuse less rapidly than the neutrons, and the high density regions would be proton rich. (AHS, 1987) derived equations for the diffusion coefficient. But (Banerjee, Chitre, 1991) [48] and (KAGMBCS, 1992) [49] derived improved equations for D_{n} that this author's own IBBN code uses. These two articles state the following equation for D_{ne}, the diffusion coefficient due to neutron/electron scattering.

$$D_{\mathrm{ne}} = \frac{3}{8}\sqrt{\frac{\pi}{2}}\frac{c}{n_{\mathrm{e}}\sigma_{\mathrm{ne}}}\frac{K_2(z)}{\sqrt{z}K_{5/2}(z)}(1-\frac{n_{\mathrm{n}}}{n_t}) \quad (4.2)$$

The articles derive this equation from the Chapman-Enskog approximation to the relativistic kinetic theory. $K_2(z)$ and $K_{5/2}(z)$ are modified Bessel functions of order 2 and 5/2, σ_{ne} is the transport cross section of the scattering and $z = m_{\mathrm{e}}/kT$. n_{n}/n_t is the neutron fraction of the total number of ALL particles. This fraction is of the order 10^{-10} and so can be ignored. The articles' equation for the diffusion coefficient due to neutron/proton scattering.

$$D_{\mathrm{np}} = \frac{3\sqrt{\pi}}{4}\sqrt{\frac{kT}{m_{\mathrm{p}}}}\frac{c}{n_{\mathrm{p}}\sigma_{\mathrm{np}}}(1-\frac{n_{\mathrm{n}}}{n_t}) \quad (4.3)$$

comes from the treatment of the neutrons and protons as hard sphere classical particles. The expression for σ_{np}:

$$\sigma_{\mathrm{np}} = \frac{\pi a_s^2}{(a_s k_w)^2 + (1.0 - \frac{1}{2}r_s a_s k_w^2)^2} + \frac{3\pi a_t^2}{(a_t k_w)^2 + (1.0 - \frac{1}{2}r_t a_t k_w^2)^2}$$

comes from s-wave scattering and includes the singlet and triplet scattering lengths a_s and a_t. and the effective ranges r_s and r_t. The wave number k_w comes from the thermal neutron momentum $\hbar k_w = \sqrt{3m_{\mathrm{n}}kT}$. From D_{np} and D_{ne} one gets the total D_{n} as

$$\frac{1}{D_{\mathrm{n}}} = \frac{1}{D_{\mathrm{ne}}} + \frac{1}{D_{\mathrm{np}}} \tag{4.4}$$

In the model in (AHS, 1987) neutron diffusion is the only function that runs during the highest temperatures. Once diffusion has homogeneously distributed the neutrons over all regions neutron/proton conversion rates and nucleosynthesis are run. The low density regions have a neutron to proton ratio much larger than one while the high density regions have a small ratio as they retain most of the protons in the universe. ^{4}He production in the low density regions depends on how quickly neutrons decay into protons first. So the final mass fraction of ^{4}He is less than the standard code result. But in the article (KMCRW, 1988) [26] Kurki-Suonio et al run a code where neutron diffusion runs both before and during nucleosythesis. In their code nucleosynthesis occurs earlier in the high density regions than the low density regions, depleting the neutrons in the high density regions. Neutrons then diffuse from the low density regions back into the high density regions. Kurki-Suonio et al's reported values of $X_{^4\mathrm{He}}$ are closer to the standard code's results than (AHS, 1987)'s values.

The distance scale r_i is defined as half the distance between recurring features in the baryon distribution. This distance expands with time and so the convention is to define r_i at a specific moment in time. (KMCRW, 1988) for instance defines r_i in light-hours/light-years at the present time. The distribution in (KMCRW, 1988)'s model is plane symmetric, with slabs of high baryon density stacked between slabs of low density a distance $2r_i$ apart from each other. If r_i is very small neutron diffusion will occur very quickly. In (KMCRW, 1988)'s code neutron/proton conversion rates run at the same time as neutron diffusion, changing the proton distribution along with the neutron distribution. For small r_i the baryon distribution becomes homogenized long before nucleosynthesis can occur. On the other hand for very large r_i diffusion would be ineffective, and the results are the same as for the codes that average between standard models of differing baryon density [46]. r_i has to have an intermediate value such that nucleosynthesis begins at the same time that diffusion has distributed the neutrons evenly over the regions. In (KMCRW, 1988) diffusion has the largest effect on the final results at an r_i of around 50 light hours at the present time.

In (KMCRW, 1988)'s results ^{4}He tends to concentrate on the boundaries between high and low density regions. Kurki-Suonio et al use a uniform grid of 20 zones from $-r_i$ to r_i, but their results imply that a finer grid is needed for the boundaries. Kurki-Suonio and Matzner follow up this article with (KM, 1989) [27] and (KMOS, 1990) [28] where their inhomogeneous code has been rewritten so that it can work for planar, cylindrical, and spherical symmetry. The code in these articles uses a 64-zone uniform grid, spread out between 0.0 and r_i in the cylindrical and spherical cases. But for density contrasts R_ρ higher than 100 and high density volume fractions f_v lower than 1/4 they have to use as many as 256 zones and 48000 timesteps to get accurate results [27]. At last in (KM, 1990) [29] Kurki-Suonio and Matzner use a code with a nonuniform grid. The grid has 64 zones spread out from $r = 0.0$ to $r = r_i$ with zones concentrated around a boundary set at $r = r_b$. To generate

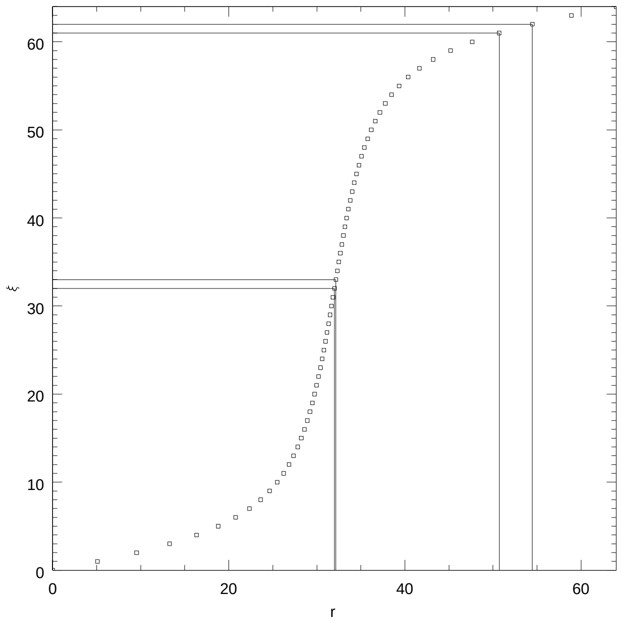

Figure 4.1: The stretching function will map integer values of ξ to values of radius r such that the r's are closely spaced in the vicinity of boundary radius r_b. In this case $r_b = 32$.

such a grid, Kurki-Suonio and Matzner define a variable $\xi(r)$ such that integer values of ξ correspond to the edges of each zone. A stretching function such as

$$\xi(r) \quad = \quad \xi(r_b) + \frac{1}{C_1}\left(1 - \frac{1}{C_3}\right)\sqrt{\frac{C_2}{C_3}}\arctan\left[(r - r_b)\sqrt{\frac{C_3}{C_2}}\right] + \frac{r - r_b}{C_1 C_2} \quad (4.5)$$

will map ξ to r such that zones near the boundary will have a width around C_1 and the far zones' size and the rate of zone-size change get determined by C_3 and C_2 respectively. For instance Figure (4.1) graphs ξ_r vs r where $r_b = 32$ and $C_1 = 1/8$. The zones close to the boundary have widths around 1/8 while the far zones have widths around 4. Kurki-Suonio and Matzner rewrite the diffusion equation as

$$\frac{\partial n_{\mathrm{n}}}{\partial t} = \frac{1}{r^p}\frac{\partial \xi}{\partial r}\frac{\partial}{\partial \xi}\left(r^p D \frac{\partial \xi}{\partial r}\frac{\partial n_{\mathrm{n}}}{\partial \xi}\right) \tag{4.6}$$

to account for ξ. Also this new version of the diffusion equation accounts for the fact that D_{np} is dependent on r. With this nonuniform grid Kurki-Suonio and Matzner can do runs with R_ρ up to 10000. But they still can't get ^{4}He, deuterium and ^{7}Li mass fractions for $\eta_{10} = 70$ that agree with observational values.

4.2 Development of the Texas IBBN Code

The Texas inhomogeneous code is built from the innovations mentioned in the articles discussed above. The results in this dissertation are for a spherically symmetric model of space. Along radius r the code divides space into 64 concentric spherical shells whose inner and outer radii are determined using Equation (4.5). The boundary r_b between high and low density regions has been set at one half the distance scale r_i and the constants C_1, C_2 and C_3 such that the shells around r_b have widths of only about $0.0025r_i$. For each shell the code keeps track of the number densities, abundances and mass fractions of the 68 different isotopes. This dissertation has results for $\eta_{10} = 3.0$. From that value of η_{10} the code determines the initial baryon number density n_{b0} for the whole model. The number densities for the high and low regions then start as

$$n_{b-low} = \frac{n_{b0}}{f_v R_\rho + (1 - f_v)} \tag{4.7}$$

$$n_{b-high} = R_\rho n_{b-low} \tag{4.8}$$

Equations (4.7) and (4.8) are such that the number densities averaged over the regions yield an overall number density of n_{b0}. The volume fraction f_v of the high density region will equal 1/8 since $r_b = 0.5r_i$. The runs use a density contrast $R_\rho = 800$.

At any given timestep the code solves the differential equation

$$\begin{aligned}\frac{\partial n(i,j)}{\partial t} &= \text{production rates} - \text{destruction rates} - 3\dot{\alpha}n(i,j) \\ &+ \frac{1}{r^p}\frac{\partial}{\partial r}\left(r^p D \frac{\partial \xi}{\partial r}\frac{\partial n(i,j)}{\partial \xi}\right)\end{aligned} \tag{4.9}$$

for the number density n of isotope # i in shell # j. The $3\dot{\alpha}n(i,j)$ term accounts for the expansion of the universe. But it's already known that an initial distance r will equal rR due to expansion. One can then rewrite this equation in comoving coordinates that eliminate the $3\dot{\alpha}n(i,j)$ term. The values of $n(i,j)$ that the code calculates will actually be $n(i,j)$ taken in a comoving value that does not change with time, but one can easily calculate the physical number density by dividing $n(i,j)$ by R^3.

In the homogeneous runs the production and destruction rates have always been written for the time derivatives of abundances $Y(i)$. For the inhomogeneous code they have to be written for the time derivatives of number densities $n(i,j)$. Equation (2.19) is the first Runge-Kutta step in calculating $Y(i)$ in the standard codes. For simplicity only the part of Equation (2.19) that applies to one two-body reaction for isotopes in the spherical shell j is written below.

$$
\begin{aligned}
i_1 + i_2 &\leftrightarrow i_3 + i_4 \\
\frac{Y_{n\alpha}(i_1,j) - Y_{n-1}(i_1,j)}{\Delta t_{n-1}} &= -\frac{1}{2}(Y_{n\alpha}(i_1,j)Y_n(i_2,j) + Y_n(i_1,j)Y_{n\alpha}(i_2,j))[i_1 i_2] \\
&\quad +\frac{1}{2}(Y_{n\alpha}(i_3,j)Y_n(i_4,j) + Y_n(i_3,j)Y_{n\alpha}(i_4,j))[i_3 i_4]
\end{aligned}
$$

Spherical shell j has baryon number density $n_b(j)$. An isotope's number density and abundance in shell j are related by

$$
n(i,j) = n_b(j)Y(i,j) \tag{4.10}
$$

One replaces $Y_{n\alpha}(i,j)$ and $Y_{n-1}(i,j)$ with $n_{n\alpha}(i,j)/n_b(j)$ and $n_{n-1}(i,j)/n_b(j)$. Presuming that $n_b(j)$ is the same for both timesteps $n-1$ and n one can rewrite the above equation as

$$
\begin{aligned}
\frac{n_{n\alpha}(i_1,j) - n_{n-1}(i_1,j)}{\Delta t_{n-1}} &= -\frac{1}{2}(n_{n\alpha}(i_1,j)Y_n(i_2,j) + Y_n(i_1,j)n_{n\alpha}(i_2,j))[i_1 i_2] \\
&\quad +\frac{1}{2}(n_{n\alpha}(i_3,j)Y_n(i_4,j) + Y_n(i_3,j)n_{n\alpha}(i_4,j))[i_3 i_4]
\end{aligned}
$$

For each of the 64 shells one can build a 68x68 matrix that can be written in terms of $Y(i,j)$ just like how the matrix in the Texas code is written in terms of $Y(i)$. The second Runge-Kutta step, which solves for $n_{n\beta}(i_1,j)$, is set up similarly.

Actually $n_b(j)$ changes with time due to diffusion. That time dependence is accounted for in the diffusion term in Equation (4.9), which has to be discretized in order to solve for the $n(i,j)$ values. The shells are defined on a grid whose points $r(j)$ correspond to the outer radii of shells j. Number densities $n(i,j)$ are regarded as the values of n at the midpoint radius between the inner and outer radii of shell j. The points $r(j)$ correspond to points in $\xi(j)$ space a distance of one unit between each other. The first space derivative in the diffusion term in (4.9) can be discretized as:

$$\begin{aligned}
\frac{\partial n}{\partial t} &= \cdots \frac{1}{r^2}\frac{\partial}{\partial r}\left(r^2 D \frac{\partial \xi}{\partial r}\frac{\partial n}{\partial r}\right) \\
\frac{\partial n}{\partial t} &= \cdots \frac{1}{r^2}\frac{\partial}{\partial r}\left[\left(r^2 D \frac{\partial \xi}{\partial r}\right)_{j-1/2} \frac{n[r(j)] - n[r(j-1)]}{1}\right]
\end{aligned}$$

Note that the coefficient $[r^2 D(\partial\xi)/(\partial r)]$ depends on r. The $(1/r^2)(\partial/\partial r)$ can be rewritten as a partial derivative of r^3. One can then write the discretization of the second space derivative as:

$$\begin{aligned}
\frac{\partial n}{\partial t} &= \cdots 3\frac{\partial}{\partial (r^3)}\left[\left(r^2 D \frac{\partial \xi}{\partial r}\right)_{j-1/2} \frac{n[r(j)] - n[r(j-1)]}{1}\right] \\
\frac{\partial n}{\partial t} &= \cdots 3\left(\frac{\left(r^2 D\frac{\partial\xi}{\partial r}\right)_j \{n[r(j+\frac{1}{2})] - n[r(j-\frac{1}{2})]\}}{r^3(j) - r^3(j-1)}\right. \\
&\qquad \left. - \frac{\left(r^2 D\frac{\partial\xi}{\partial r}\right)_{j-1} \{n[r(j-\frac{1}{2})] - n[r(j-\frac{3}{2})]\}}{r^3(j) - r^3(j-1)}\right)
\end{aligned}$$

For an isotope i the densities $n[r(j+1/2)]$, $n[r(j-1/2)]$ and $n[r(j-3/2)]$ are defined as $n(i,j+1)$, $n(i,j)$ and $n(i,j-1)$ respectively. The coefficient $[r^2 D(\partial\xi)/(\partial r)]_j$ is calculated at $r(j)$. One can apply this discretization to a fully implicit version of the diffision part of (4.9). That part of (4.9) for the first Runge-Kutta step is then

$$\frac{n_{n\alpha}(i,j) - n_{n-1}(i,j)}{\Delta t_{n-1}} = \cdots - \frac{3\left(r^2 D\frac{\partial\xi}{\partial r}\right)_j}{r^3(j) - r^3(j-1)} n_{n\alpha}(i,j+1)$$

$$+3\frac{\left(r^2D\frac{\partial\xi}{\partial r}\right)_j+\left(r^2D\frac{\partial\xi}{\partial r}\right)_{j-1}}{r^3(j)-r^3(j-1)}n_{n\alpha}(i,j)$$
$$-\frac{3\left(r^2D\frac{\partial\xi}{\partial r}\right)_{j-1}}{r^3(j)-r^3(j-1)}n_{n\alpha}(i,j-1)$$

The second Runge-Kutta step is written similarly. Any baryons that flow out beyond the distance scale are assumed to be replenished by baryons flowing in from other sets of spherical shells, and $r(0) = 0$ is the center of the shells. So the code uses reflective boundary conditions at the endpoints of the grid.

$$\begin{aligned}
\frac{n_{n\alpha}(i,1)-n_{n-1}(i,1)}{\Delta t_{n-1}} &= \cdots - \frac{3\left(r^2D\frac{\partial\xi}{\partial r}\right)_1}{r^3(1)-r^3(0)}n_{n\alpha}(i,2) \\
&\quad + \frac{3\left(r^2D\frac{\partial\xi}{\partial r}\right)_1}{r^3(1)-r^3(0)}n_{n\alpha}(i,1) \\
\frac{n_{n\alpha}(i,64)-n_{n-1}(i,64)}{\Delta t_{n-1}} &= \cdots + \frac{3\left(r^2D\frac{\partial\xi}{\partial r}\right)_{64}}{r^3(64)-r^3(63)}n_{n\alpha}(i,64) \\
&\quad - \frac{3\left(r^2D\frac{\partial\xi}{\partial r}\right)_{63}}{r^3(64)-r^3(63)}n_{n\alpha}(i,63)
\end{aligned}$$

where $r(64) =$ distance scale r_i. The above equations can be applied to the diffusion of any isotope i. In my inhomogeneous code only neutrons, $i = 1$, diffuse.

The articles mentioned above used codes that solved the diffusion part of Equation (4.9) separately from the nuclear reaction part. In a recent article Kainulainen, et al [45] were able to solve Equation (4.9) all at once. In the Texas IBBN code the 64 matrices of each of the shells built from the nuclear reactions and weak decay are strung together into one large matrix. The rows corresponding to free neutrons in each section will have the only components that connect the matrices together, with nonzero components that couple $n(1,j)$ with $n(1,j+1)$ and $n(1,j-1)$. The code solves for this giant matrix equation for the number densities as the Texas code solves its matrix equation for the abundances. (Fortunately the sparseness of the large matrix enabled this author to write code that didn't require defining a 4352x4352 matrix in order to solve the equation.) After both Runge-Kutta steps get done and new values of $n(i,j)$ get calculated the code determines the new baryon number density $n_b(j)$ of each shell using

$$n_b(j) = \sum_{i=1}^{68} A_i n(i,j)$$

and from $n_b(j)$ and $n(i,j)$ the code can calculate $Y(i,j)$. At any given time the abundance $Y_{av}(i)$ of isotope i in the whole model can be calculated from $Y(i,j)$ using.

$$Y_{av}(i) = \frac{\sum_{j=1}^{64} n(i,j)[r^3(j) - r^3(j-1)]}{\sum_{j=1}^{64} n_b(j)[r^3(j) - r^3(j-1)]}$$

These overall abundances are compared with the abundances found in observations, and in the Texas code.

4.3 Results

Figures (4.2a) and (4.2b) show contour maps of $\log[Y(\mathrm{d})/Y(\mathrm{p})]$ and $X_{^4\mathrm{He}}$ respectively when the Texas IBBN code is run with the values for R_ρ and f_v mentioned before. The code is run for varying values of baryon-to-photon ratio η and distance scale r_i. For the next few paragraphs the chapter describes the results gotten when the value of r_i is varied for a set $\eta_{10} = 3.0$. Table (4.1)

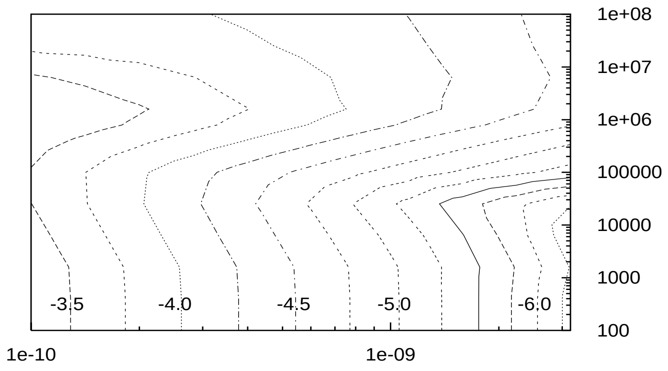

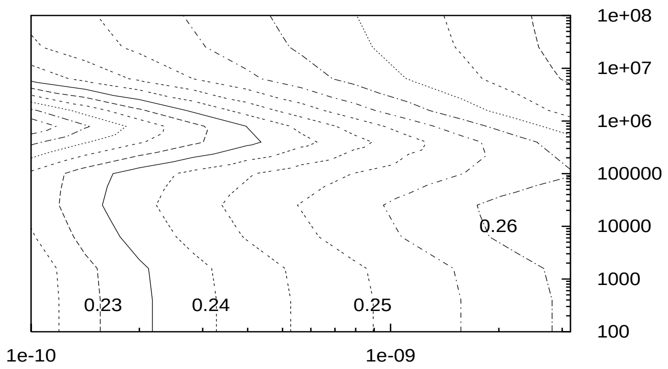

Figure 4.2: The log of abundance $Y(\mathrm{d})/Y(\mathrm{p})$ (4.2a), and mass fraction $X_{^4\mathrm{He}}$ (4.2b) in the IBBN code. The horizontal axis is for baryon-to-photon ratio η and the vertical axis is for distance scale r_i in centimeters at temperature $T =$ 100 GK.

r_i	$10^{-4}X_{\rm d}$	$X_{^4{\rm He}}$
10^2	1.22571163	0.239029657
1.58489 $\times 10^3$	1.20243159	0.239369667
2.51189 $\times 10^4$	0.83557457	0.243663794
10^5	0.95704758	0.241847338
7.94328 $\times 10^5$	3.00408002	0.229781933
6.30957 $\times 10^6$	2.58745378	0.250711334

Table 4.1: The most interesting mass fractions of deuterium and ^{4}He for various values of r_i. Here $\eta_{10} = 3.0$, $f_v = 1/8$, and $R_\rho = 800.0$.

lists the mass fractions of ^{4}He and deuterium for the values of r_i looked at, those values giving the most interesting final results for ^{4}He.

4.3.1 r_i = 100 cm

A run with $r_i = 100$ cm corresponds to the bottom of Figures (4.2a) and (4.2b). Figure (4.4) is a three dimensional graph showing the evolution over time of the neutron and proton number densities ($n_{\rm n}(j)$) and ($n_{\rm p}(j)$), and four times the ^{4}He number density ($4 \times n_{^4{\rm He}}(j)$) in shell j. The number densities are measured using comoving distances, and normalized using the initial baryon number density n_{b0} of the entire model. Temperature T runs along the x-axis while r (normalized to have a range of 0.0 to 64.0) runs along the y-axis. The graphs for $n_{\rm n}(j)$ and $n_{\rm p}(j)$ start out with the high and low values set by the parameters. But diffusion rapidly depletes the high density region and fills the low density region. By the time $T = 60$ GK diffusion has nearly homogenized the baryon distribution.

Figure (4.3) graphs r_i vs. T showing how r_i increases due to the expansion of the universe. The figure also shows the diffusion length $d_l = \sqrt{D_{\rm n} t}$ measured at the center and the outside edge of the model (shells 3 and 62).

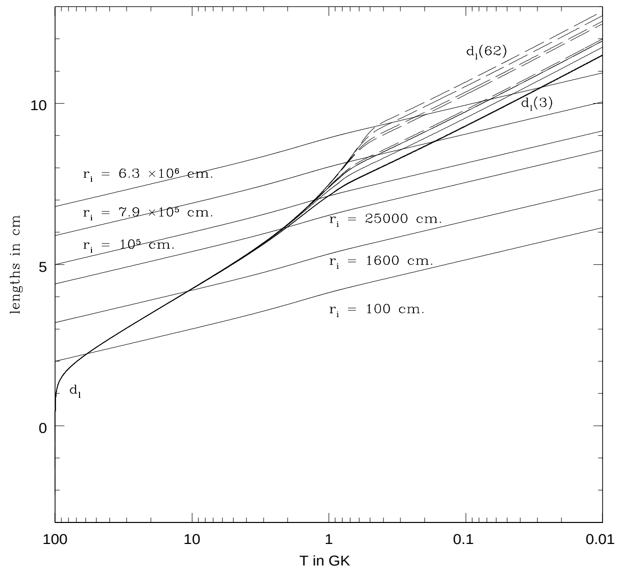

Figure 4.3: The diffusion lengths d_l for shells 3 and 62 compared with the distance scales r_i looked at in this chapter. Diffusion becomes significant when a graph for r_i intersects the graph for d_l

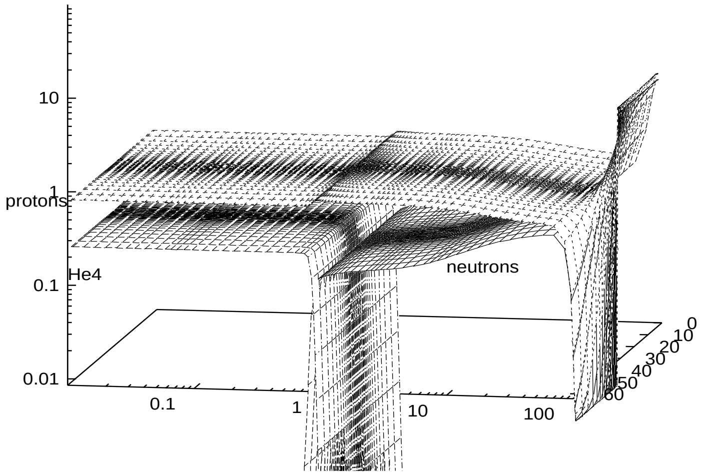

Figure 4.4: $n_{\rm n}$, $n_{\rm p}$ and $4n_{^4{\rm He}}$ for $r_i = 100$ cm. The $x-$axis is r scaled to 64, the $y-$axis is T in GK, and the $z-$axis is n_i/n_{b0}.

Using dimensional analysis one can define $\sqrt{D_{\rm n} t}$ as an approximate measure of how far out a range from a given point diffusion can affect at a time t since the start of the run. For the highest temperatures the large electron number density $n_{\rm e}$ in Equation (4.2) makes $D_{\rm ne}$ considerably smaller than $D_{\rm np}$. So $D_{\rm ne}$ dominates $D_{\rm n}$ in Equation (4.4) and the diffusion length is nearly the same all through the model. Figure (4.3) shows that this r_i starts out small enough that d_l overtakes it when $T =$ around 60 GK. At that temperature and higher the neutron-proton conversion reactions still occur very rapidly. As quickly as diffusion depletes neutrons in the high density region the conversion reactions change protons to neutrons, and the reverse applies to the low density region.

Figure (4.5a) shows the diffusion rates and the conversion rates for shell 3, a shell near the center of the model and one that starts out with a high density. (The rates are normalized to both n_{b0} and the expansion rate, so that the y-axis here is dimensionless.) Figure (4.5a) shows that the diffusion rate from shell 3 to shell 4 outpaces the rate from shell 2 to shell 3. A closeup of the conversion rates shown in Figure (4.5b) shows that the conversion of protons to neutrons is running more rapidly than the conversion of neutrons to protons. The difference between the rates appears small when compared to the conversion rates themselves, but the difference is still of comparable magnitude to the difference between the diffusion rates in Figure (4.5a). The protons are being rapidly converted to neutrons and then diffused out to the outer shells.

Figure (4.6a) shows the opposite effects occuring in shell 62, near the outer edge of the model and with a initial low baryon density. One can see in Figure (4.6a) that the neutron flow from shell 61 into shell 62 exceeds the flow from 62 to 63, resulting in an increase in neutron number density there.

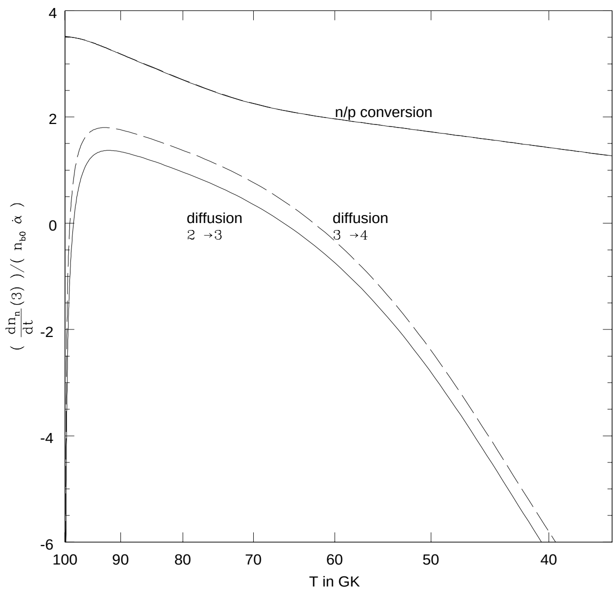

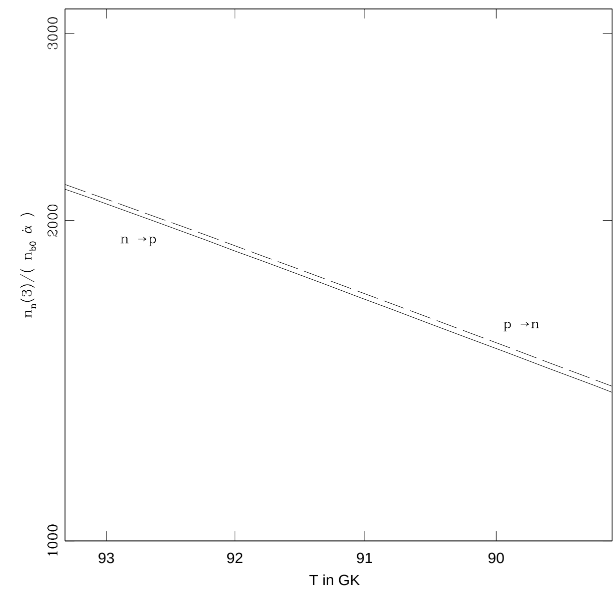

Figure 4.5: The neutron diffusion rates into and out of shell 3 compared with the neutron-proton conversion rates in shell 3. Here $r_i = 100$ cm. (4.5b) shows a closeup of the conversion rates, where the p $\rightarrow$ n rates occur faster than the n $\rightarrow$ p rates.

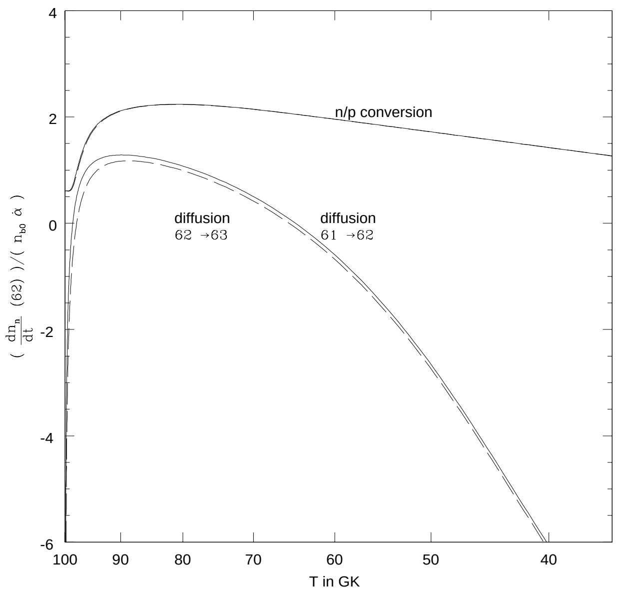

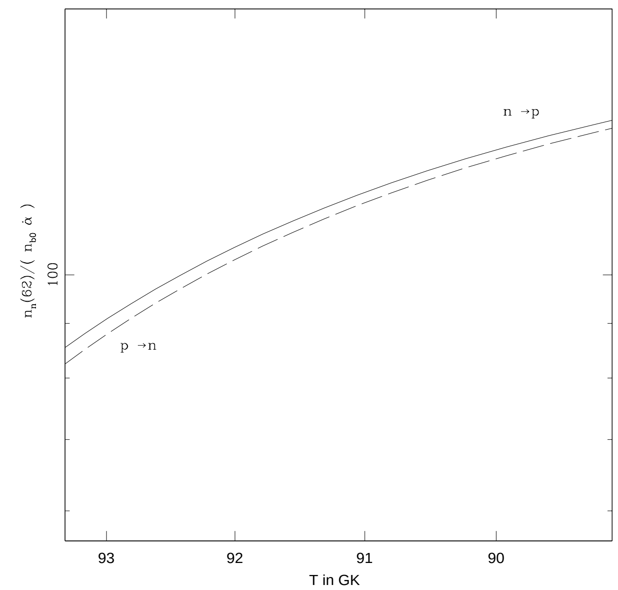

Figure 4.6: The neutron diffusion rates into and out of shell 62 compared with the neutron-proton conversion rates in shell 62. Here $r_i = 100$ cm. (4.6b) shows a closeup of the conversion rates, where the n $\rightarrow$ p rates occur faster than the p $\rightarrow$ n rates.

The closeup on the conversion rates shown in Figure (4.6b) show that more neutrons are being converted to protons than protons to neutrons, filling low density shells with protons as well. For $T < 60$ GK, the IBBN code behaves like a standard code. In Figures (4.5a) and (4.6a) one can see that the conversion rates start out high in the high density shell 3 and low in the low density shell 62, but they fall and rise respectively to the same graphs that they'd have in a standard code by the time that $T = 60$ GK.

4.3.2 $r_i = 1600$ cm

When the initial distance scale is increased to $r_i =$ around 1600 cm. $X_{^4\mathrm{He}}$ at a given value of η_{10} starts to increase from its homogeneous value, as shown in the shifts to the left of the contour lines in Figure (4.2b). Figures (4.7) show opposite views of the three dimensional graphs of n_n, n_p and $4 \times n_{^4\mathrm{He}}$ corresponding to this distance scale. As in Figure (4.4), diffusion eventually homogenizes n_n.(Figure (4.7b) more clearly illustrates this.) But diffusion occurs more slowly for this longer distance scale. Up to around 30 GK for the high density shells and 40 GK for the low density shells the evolution of n_n and n_p is determined by the neutron-proton coversion rates instead of diffusion.

Figure (4.8a) shows the conversion rates and diffusion rates for shell 3, and Figure (4.9a) shows those results for shell 62. The graphs of the conversion rates run parallel to the graphs they'd have in a standard code, but they're larger for shell 3 and smaller for shell 62, because of the larger/smaller number densities of neutrons and protons the shells start out with. When the diffusion rates become significant, though, the conversion rates start to shift more towards their standard model values. In Figure (4.9a) the conversion

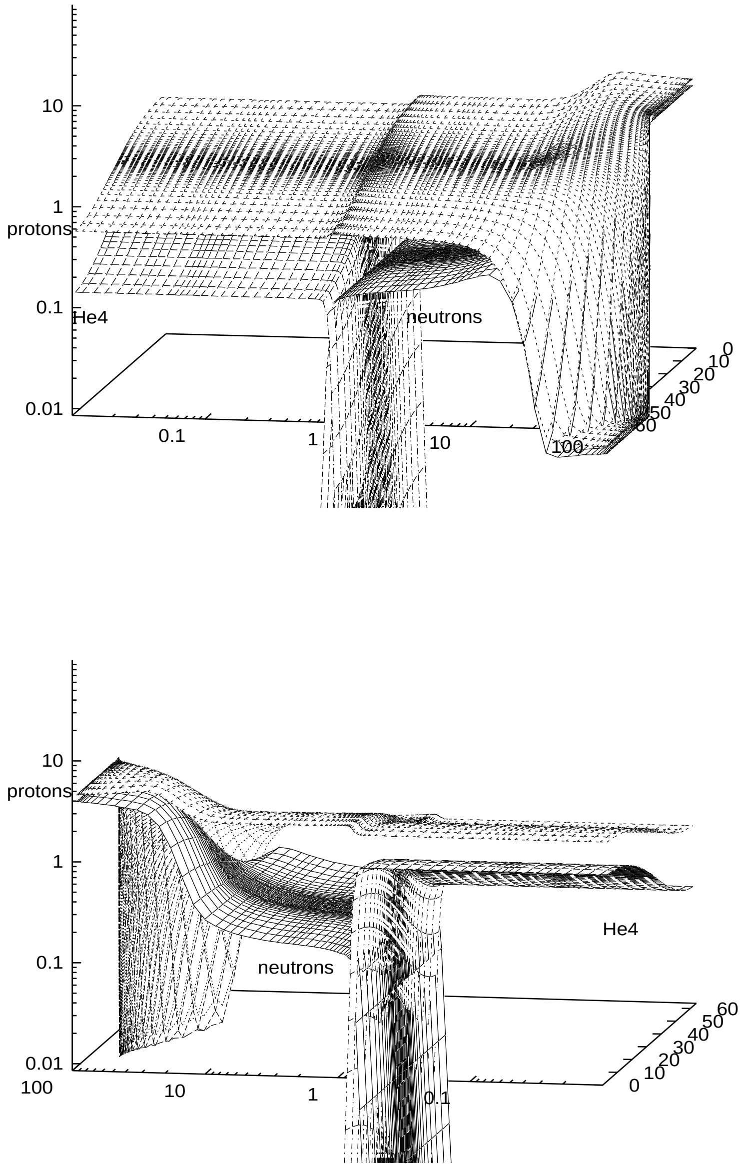

Figure 4.7: $n_{\rm n}$, $n_{\rm p}$ and $4n_{^4\rm He}$ for $r_i = 1600$ cm. From here on, the viewpoint in (4.7b) will be used.

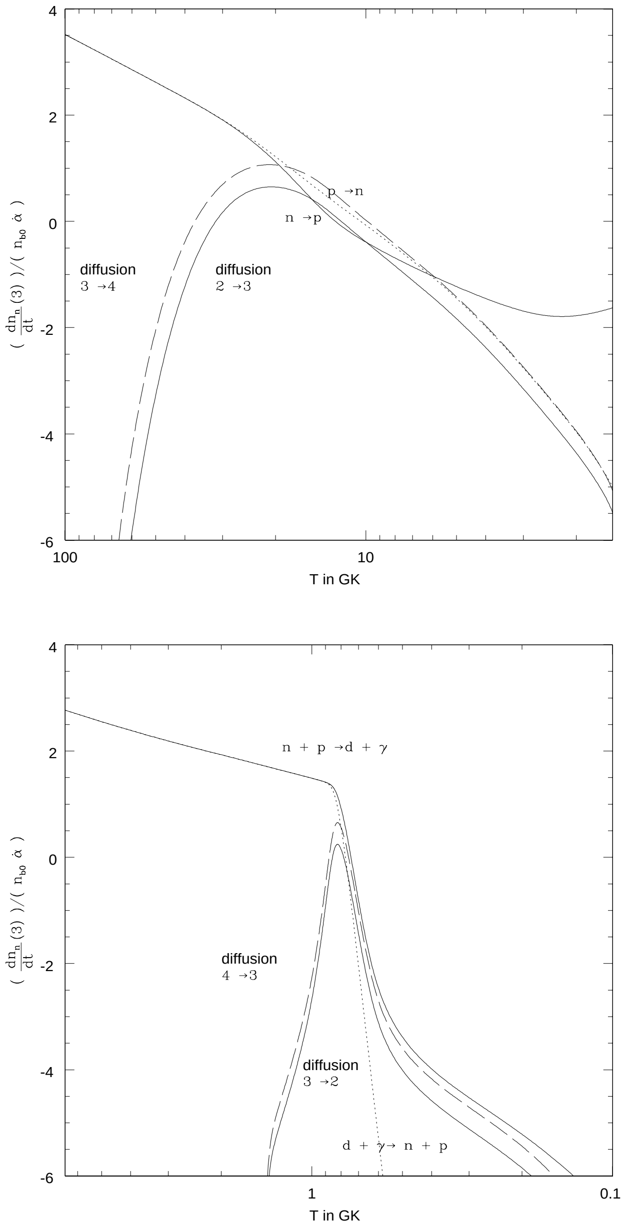

Figure 4.8: The neutron diffusion rates into and out of shell 3 compared with the neutron-proton conversion rates in shell 3 (4.8a), and the back diffusion rates compared with the nuclear reaction rate n + p $\leftrightarrow$ d + γ (4.8b). Here r_i = 1600 cm.

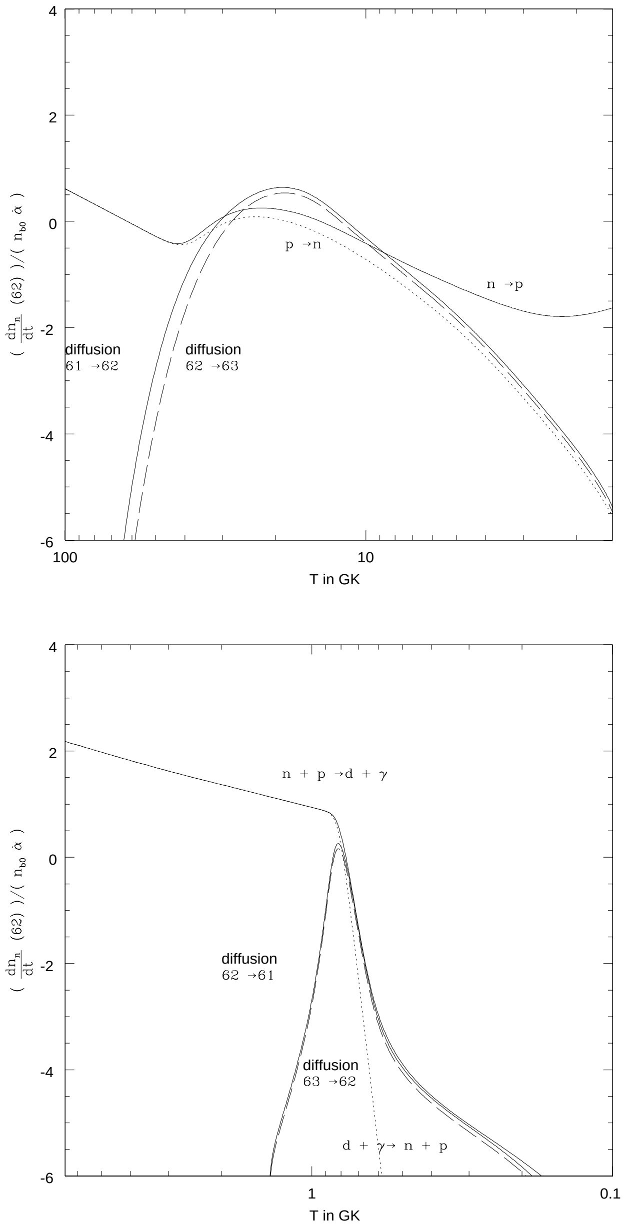

Figure 4.9: The neutron diffusion rates into and out of shell 62 compared with the neutron-proton conversion rates in shell 62 (4.9a), and the back diffusion rates compared with the nuclear reaction rate n + p $\leftrightarrow$ d + γ (4.9b). Here r_i = 1600 cm.

rates start rising by 40 GK when the difusion rates reach the same magnitude as the conversion rates. In Figure (4.8a) the neutron-proton conversion rates starts to dip to their standard model values just when the diffusion rates reach their maximums. By the time $T = 20$ GK the neutron to proton rate is visibly smaller than the proton to neutron rate in Figure (4.8a). So again protons are being converted to neutrons which flow from the high density shells to the low, where the conversion rates can then convert them back to protons. But at these lower temperatures the conversion reactions don't run rapidly enough to homogenize the proton number density. Figure (4.3) shows that for $r_i =$ around 1600 cm. that the diffusion length reaches the distance scale at about $T = 10$ GK. The conversion rates already fall out of equillibrium at 13 GK. So when in Figures (4.7a) and (4.7b) n_{n} has reached a homogeneous value n_{p} still varies depending on the shell.

Because of the larger proton number densities remaining in the inner shells the rate of fusion of protons to neutrons into deuterium, n + p $\to$ d + γ, goes much faster in the inner shells than the outer shells. Because that nuclear reaction runs faster all the subsequent nuclear reactions run faster as well. The rate of n + p $\to$ d + γ begins to significantly alter n_{n} at around 0.9 GK. Near that temperature n_{n} has the same value in all the shells, but for any small interval in time n + d $\to$ d + γ converts a greater number of neutrons to deuterium nuclei in the inner shells than the outer shells. n_{n} will start to have a smaller value in the inner shells, causing neutrons to diffuse back into the inner shells. Figure (4.8b) shows the forward and reverse rates of n + p $\to$ d + γ. The rates themselves start out very large, but are nearly equal, to the point that their net difference is initially too small to have a noticible effect on n_{n}. Figure (4.8b) shows the rates fall out of equilibrium at 0.9 GK, and the forward rate and reverse rate then have a large difference between them. At the same time, the diffusion rates have risen in magnitude again almost as much as before, but now the direction of the flow has reversed. Figure (4.8b) shows that the rate of flow from shell 4 to shell 3 is higher in magnitude than from shell 3 to shell 2. As fast as these flow rates go, the deuterium production rate go faster. So all the neutrons flowing back into shell 3 quickly get converted to deuterium, and then ultimately to ^{4}He nuclei. Figure (4.9b) shows the equivalent rates for shell 62. Here the forward and reverse rates of n + p $\rightarrow$ d + γ indeed are smaller than in shell 3. Ultimately nearly all neutrons are incoporated into ^{4}He nuclei and as shown in Figure (4.7a) more ^{4}He is made in the shells with larger n_{p} than the other shells. Still, the final mass fraction, calculated from averaging the densities over the shells' volumes, increases only slightly from the homogeneous case for $r_i = 1600$ cm.

4.3.3 r_i = 25000 cm

When $r_i = 25000$ cm. $X_{^4\mathrm{He}}$ reaches a maximum along the line for $\eta_{10} = 3.0$ in Figure (4.2b). Figure (4.3) shows that r_i doesn't expand past d_l until around 1.2 GK, considerably later on from when the neutron-proton conversion reactions fall out of equilibrium. Figure (4.10) shows the number densities from the inner shells' side of the radius axis. n_{n} decreases steadily due to the conversion reactions, and then has a much steeper fall due to diffusion. n_{p} on the inner shells' side has no visible decrease.

Figure (4.11a) shows the diffusion rates and conversion rates for shell 3 and for $r_i = 25000$ cm. The diffusion rates peak at around 4 GK and at that temperature the p $\rightarrow$ n rates are already low enough such that they can

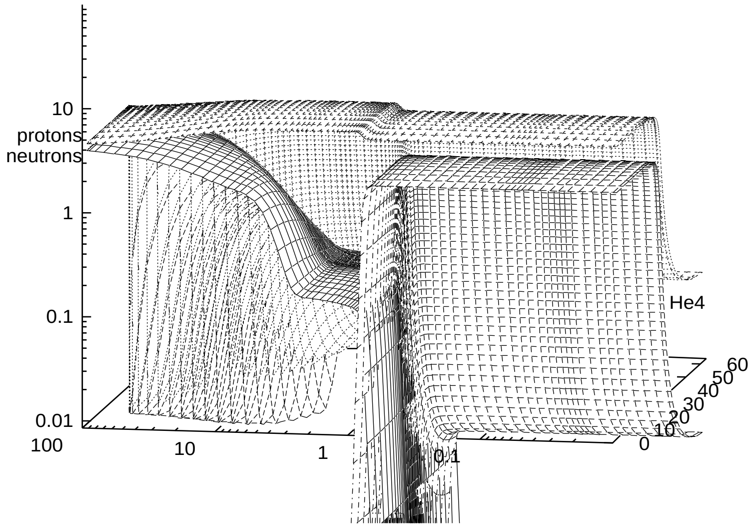

Figure 4.10: $n_{\rm n}$, $n_{\rm p}$ and $4n_{^4{\rm He}}$ for $r_i = 25000$ cm. $n_{\rm n}$ reaches a homogeneous value at around $T = 3.0$ GK.

never get larger than the n $\rightarrow$ p rates due to diffusion. Very little if any of the protons in the inner shells get converted to neutrons and then transferred to the outer shells. In Figure (4.12a) the influx of neutrons into shell 62 causes the n $\rightarrow$ p rates to rise to its homogeneous values and so this outer shell fills up with protons. But the neutrons come in so late in the run that the n $\rightarrow$ p reactions cannot produce enough protons to keep up with the neutrons coming in.

Figures (4.11b) and (4.12b) show the back diffusion rates and the forward and reverse rates of n + p $\leftrightarrow$ d + γ for shell 3 and shell 62 respectively. The rate for n + p $\rightarrow$ d + γ in shell 3 and shell 62 respectively are even larger and smaller than the corresponding rates for $r_i = 1600$ cm, leading to

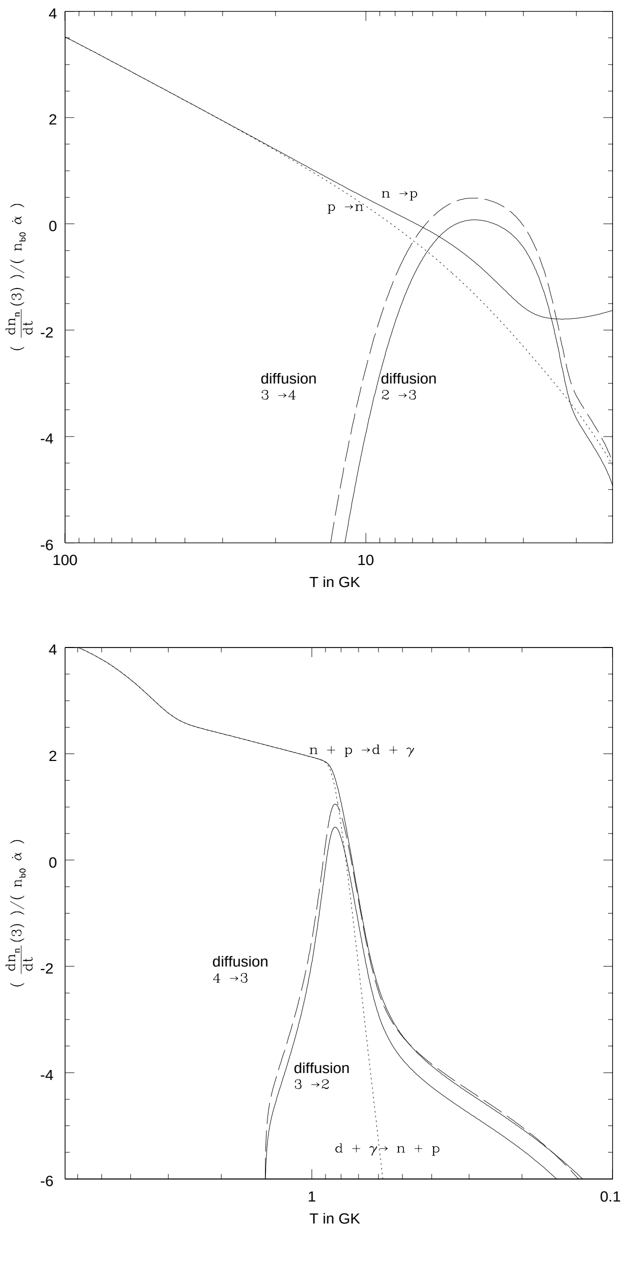

Figure 4.11: The neutron diffusion rates into and out of shell 3 compared with the neutron-proton conversion rates in shell 3 (4.11a), and the back diffusion rates compared with the nuclear reaction rate n + p $\leftrightarrow$ d + γ (4.11b). Here $r_i = 25000$ cm.

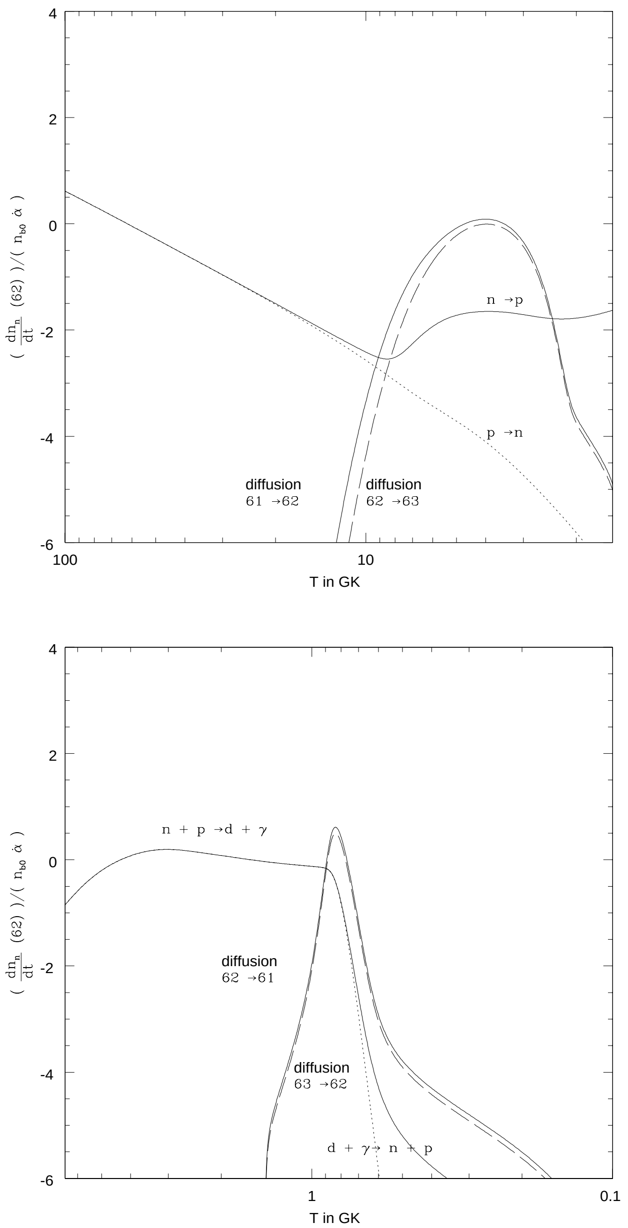

Figure 4.12: The neutron diffusion rates into and out of shell 62 compared with the neutron-proton conversion rates in shell 62 (4.12a), and the back diffusion rates compared with the nuclear reaction rate n + p $\leftrightarrow$ d + γ (4.12b). Here $r_i = 25000$ cm.

faster depletion of the neutrons in the inner shells than the outer. So the back diffusion rates arise, with larger magnitudes for $r_i = 25000$ cm than for $r_i = 1600$ cm. The back diffusion rates in shell 62 are in fact larger in magnitude than the rate for n + p → d + γ. Thus the neutrons in the outer shells do not combine with the shells' protons to form deuterium and ultimately ^{4}He but instead flow back into the inner shells where nucleosynthesis uses them to form ^{4}He with the protons in the inner shell. Figure (4.10) shows that in the outer shells nucleosynthesis produces a minimal amount of ^{4}He and doesn't deplete any of the protons in that shell. Whereas the inner shells have a large production of ^{4}He, made from neutrons from all the shells. The larger back diffusion rates also make nucleosynthesis occur earlier in the model. So when nucleosynthesis occurs, n_n is at a value that's the same in all shells and a value higher than in models with smaller r_i. The final mass fraction ^{4}He reaches a maximum value of 0.243664 at this r_i.

4.3.4 $r_i = 10^5$ cm

Figures (4.13) to (4.15) correspond to the case when $r_i = 10^5$ cm. At that distance scale and for $\eta_{10} = 3.0$ $X_{^4\mathrm{He}}$ has started to decrease. Figure (4.13) shows the number densities for this distance scale. n_p in the inner shells looks nearly unchanged from n_p in Figure (4.10). On the outer shells' side (not visible in Figure (4.13)) n_p has a period of time where it increases, but for not as long as in the case for $r_i = 25000$ cm. The graph for n_n shows that diffusion occurs later, but n_n still reaches a homogeneous value before nucleosynthesis.

Figure (4.14a) shows the neutron/proton conversion rates and the neutron diffusion rates for shell 3, and Figure (4.15a) shows these rates for shell

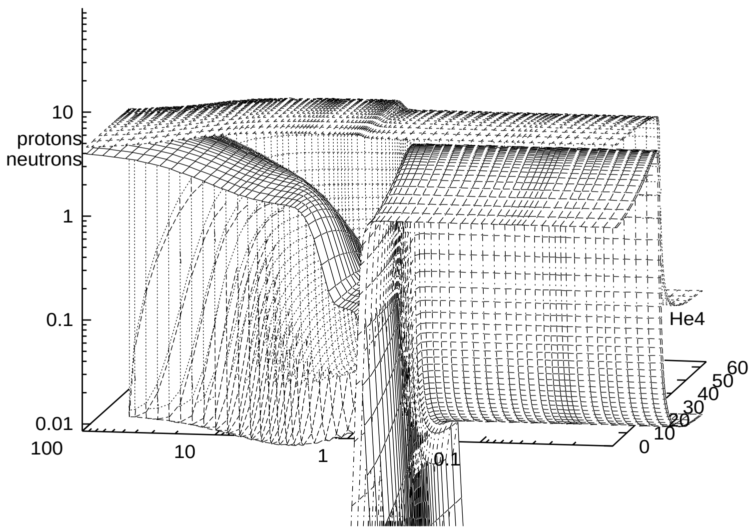

Figure 4.13: n_{n}, n_{p} and $4n_{^4\mathrm{He}}$ for $r_i = 10^5$ cm. n_{n} reaches a homogeneous value at around $T = 2.0$ GK.

62. The diffusion rates peak at near 4 GK for the case of $r_i = 25000$ cm. In that preceding case the diffusion rates grew large much later than the time when the conversion rates fell out of equilibrium, and so the proton to neutron conversion rate in shell 3 was not affected by the diffusion rates. The diffusion rates peak even later when $r_i = 10^5$ cm, at around 2 GK. The graph of the proton-to-neutron conversion rate in shell 3 is then the same in both Figures (4.14a) and Figure (4.11a). The later time for diffusion allows the proton number density n_{p} in shell 3 to increase from before, but only due to neutron decay.

Figure (4.3) shows that for $r_i = 10^5$ cm the diffusion lengths for the inner shells and the outer shells have a nontrivial difference between them for

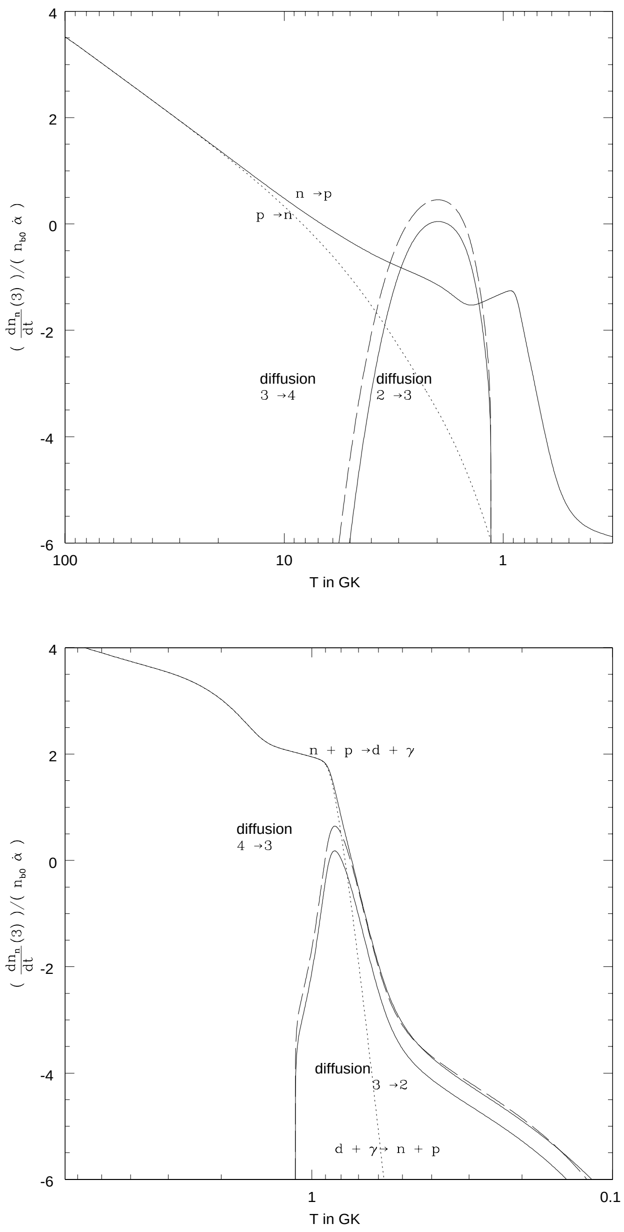

Figure 4.14: The neutron diffusion rates into and out of shell 3 compared with the neutron-proton conversion rates in shell 3 (4.14a), and the back diffusion rates compared with the nuclear reaction rate n + p $\leftrightarrow$ d + γ (4.14b). Here $r_i = 10^5$ cm.

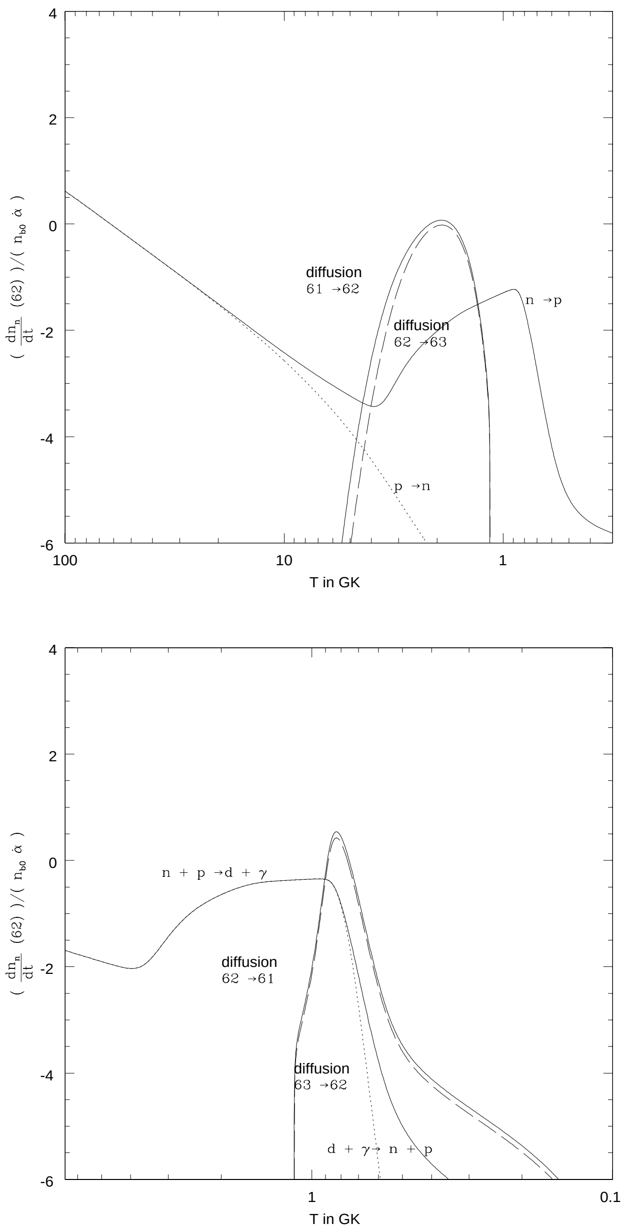

Figure 4.15: The neutron diffusion rates into and out of shell 62 compared with the neutron-proton conversion rates in shell 62 (4.15a), and the back diffusion rates compared with the nuclear reaction rate n + p $\leftrightarrow$ d + γ (4.15b). Here $r_i = 10^5$ cm.

temperatures lower than 1.5 GK. At 1.1 GK these diffusion lengths catch up with the expanding distance scale. Figure (4.14b) shows the back diffusion rates and the reaction rates for n + p $\leftrightarrow$ d + γ for shell 3, and (4.15b) shows those same rates for shell 62. Up to now, a larger distance scale led to more protons remaining in shell 3. So the rate of deuterium production was larger for r_i = 25000 cm (Figure (4.11b)) than for r_i = 1600 cm (Figure (4.8b)). But the rate of deuterium production in (4.14b) is about the same as in (4.11b) when nucleosynthesis occurs because shell 3 for r_i = 1600 cm has nearly the same amount of protons as shell 3 r_i = 25000 cm. As with the smaller distance scales the neutrons in the outer shells diffuse back into the inner shells. But the neutrons take longer to diffuse back. During that time some neutrons decay into protons instead. The amount of neutrons diffusing back to the inner shells is less than for smaller distance scales, and so fewer neutrons are incorporated into 4He nuclei.

Further, r_i is at a value where the neutrons diffusing back can't quite reach the innermost shells. Figure (4.16) compares the final number density of $n_{^4\mathrm{He}}$ of ^{4}He in each shell for the six values of r_i discussed in this dissertation. Since neutrons can still reach all shells in back diffusion for r_i = 25000 cm $n_{^4He}$ has a uniform value in the inner shells. For $r_i = 10^5$ cm the neutrons reach only shells close to the boundary. So $n_{^4\mathrm{He}}$ is larger at the boundary and decreases with decreasing radius. In the outermost shells some neutrons remain long enough to undergo nucleosynthesis with the protons already there. So the outermost shells have slightly more ^{4}He production for the larger r_i. Table (4.1) lists the final total mass fraction of ^{4}He as around 0.241847 for $r_i = 10^5$ cm, lower than for $r_i = 25000$ cm.

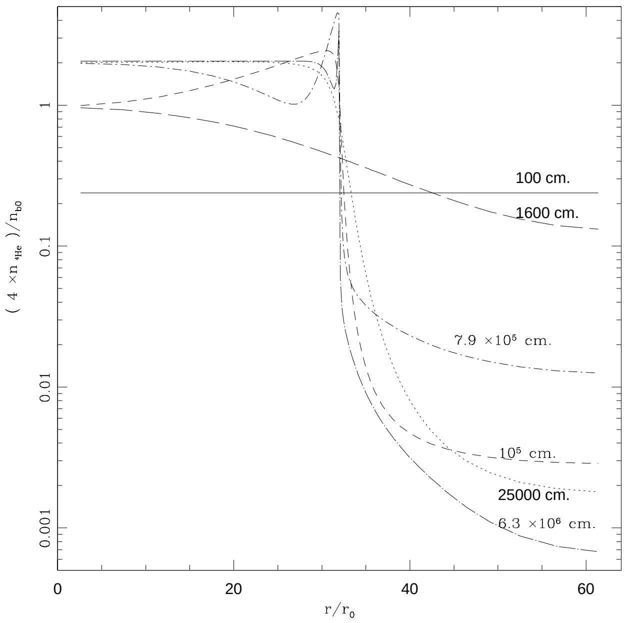

Figure 4.16: $4n_{^4\mathrm{He}}$ at the end of the run, as a function of radius r. The value of the distance scale r_i determines the shape of each graph.

4.3.5 $r_i = 7.9 \times 10^5$ cm

$X_{^4\mathrm{He}}$ keeps decreasing as r_i increases, until it bottoms out when $r_i =$ about 7.9×10^5 cm. Figure (4.17a) shows the number densities of neutrons, protons and ^{4}He nuclei for this value of the distance scale. Figure (4.17a) seems to have no time period where the neutrons have a homogeneous distribution. Figure (4.17b) graphs n_n all by itself, for a larger range of the $z-$axis. This figure shows that by the time of nucleosynthesis diffusion has not quite raised n_n in the outer shells enough to attain a homogeneous value, and n_n for the innermost shells have been only slightly reduced.

Figure (4.18a) shows the diffusion rates and conversion rates in shell 3 for this r_i, and Figure (4.19a) shows the corresponding rates for shell 62.

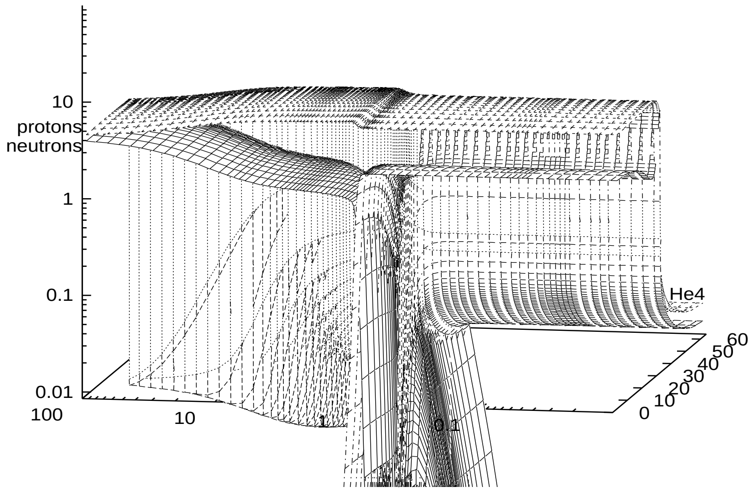

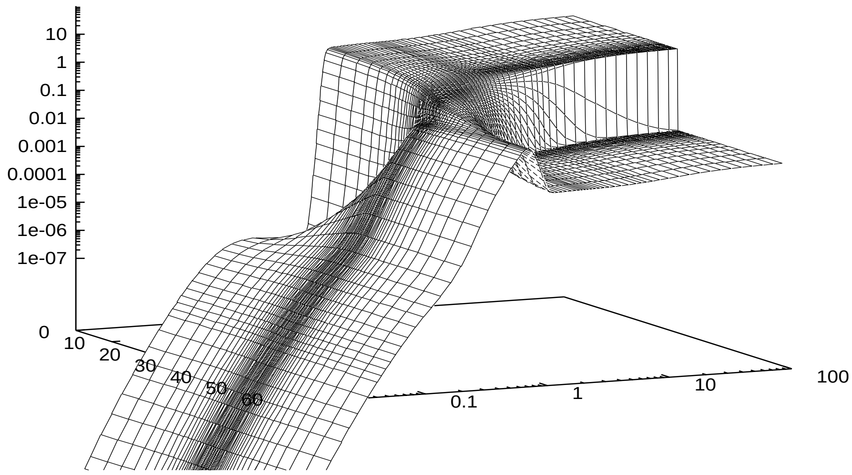

Figure 4.17: n_n, n_p and $4n_{^4\mathrm{He}}$ for $r_i = 7.9 \times 10^5$ cm. n_n doesn't reach a a homogeneous value. (4.17b) shows n_n alone in a better illustration of the graph's details.

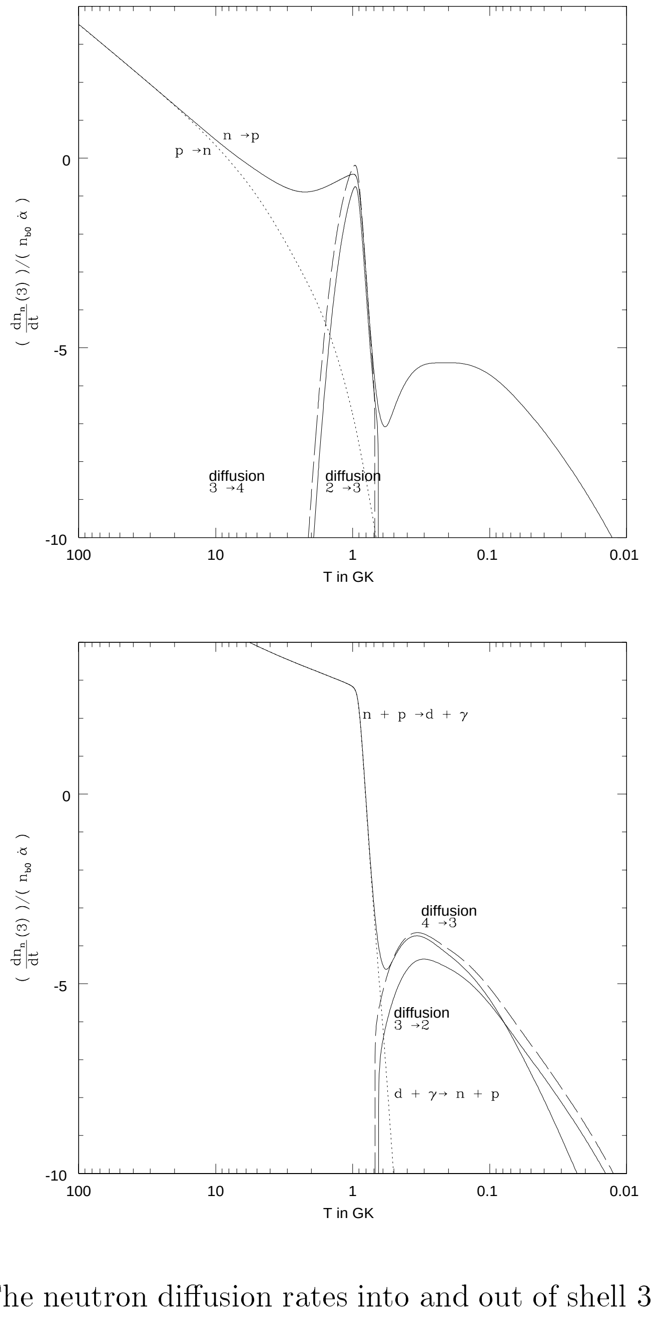

Figure 4.18: The neutron diffusion rates into and out of shell 3 compared with the neutron-proton conversion rates in shell 3 (4.18a), and the back diffusion rates compared with the nuclear reaction rate n + p $\leftrightarrow$ d + γ (4.18b). Here $r_i = 7.9 \times 10^5$ cm.

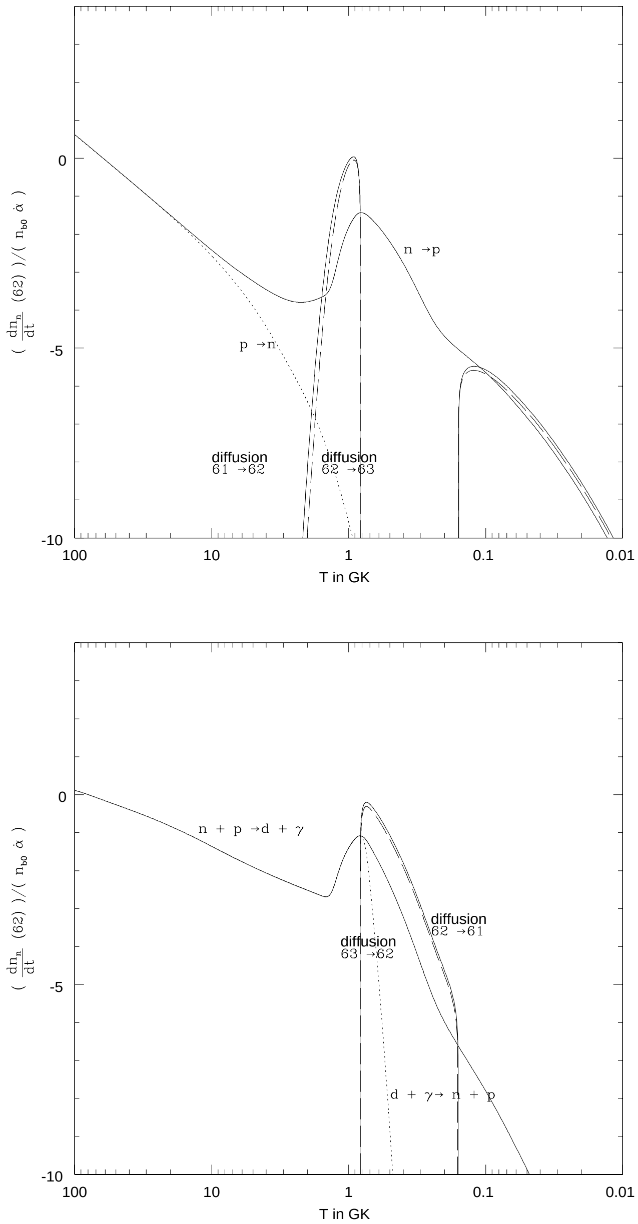

Figure 4.19: The neutron diffusion rates into and out of shell 62 compared with the neutron-proton conversion rates in shell 62 (4.19a), and the back diffusion rates compared with the nuclear reaction rate n + p $\leftrightarrow$ d + γ (4.19b). Here $r_i = 7.9 \times 10^5$ cm.

Diffusion now occurs so late that nucleosynthesis happens at the same temperature as when the diffusion rates peak in both shells. This late diffusion leads to the larger value of n_{n} in the inner shells shown in Figure (4.17b). The neutron to proton conversion rate in Figure (4.18a) then has a larger value when nucleosynthesis occurs than for any r_i smaller than 7.9×10^5 cm. So nucleosynthesis occurs much more rapidly in shell 3 than for smaller r_i, illustrated in the steeper fall of the conversion rate graph in Figure (4.18a). In Figure (4.19a) diffusion of neutrons into shell 62 causes the neutron to proton conversion rate to rise, but the rate doesn't reach as high a value when nucleosynthesis occurs as it does for smaller r_i. So nucleosynthesis occurs much slower than before, as illustrated in the more gradual fall in the conversion rate shown in Figure (4.19a).

The more rapid nucleosynthesis in the inner shells depletes the neutrons in the inner shells until n_{n} is considerably smaller in the inner shells than the outer shells. Back diffusion then occurs, first in the outer shells such as shell 62, shown in Figure (4.19b), and later on in the inner shells such as shell 3, as shown in Figure (4.18b). The influx in neutrons causes an increase in both the rates for $\mathrm{n} \to \mathrm{p}$ in Figure (4.18a) and $\mathrm{n} + \mathrm{p} \to \mathrm{d} + \gamma$ in Figure (4.18b), until both graphs match the corresponding graphs in Figures (4.19a) and (4.19b).

Figure (4.20) shows the neutron number densities n_{n} as functions of temperature for this chapter's six distance scales r_i, with the solid lines for n_{n} of shell 3 and the broken lines for n_{n} of shell 62. For $r_i = 100$ cm, 1600 cm, 25000 cm and 10^5 cm the neutron number densities in each shell eventually reach homogeneous values some time before nucleosynthesis and have similar graphs after nucleosynthesis. But for $r_i = 7.9 \times 10^5$ cm n_{n} in shell 3 is depleted by nucleosynthesis before diffusion can have a significant effect on it, while n_{n}

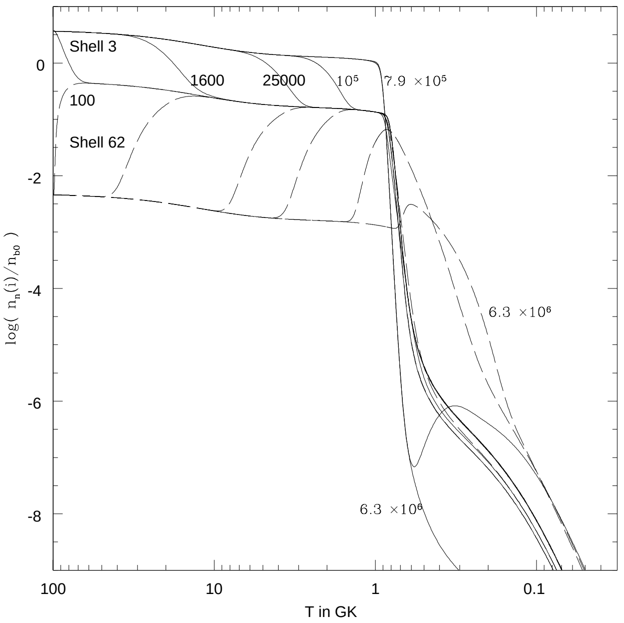

Figure 4.20: For the first four values of r_i the graphs for $n_{\rm n}$ of shells 3 and 62 come together to a homogeneous value before nucleosynthesis. But nucleosynthesis occurs before the neutrons can homogenize for the two largest values of r_i, and so the graphs for $n_{\rm n}$ diverge.

in shell 62 increases due to diffusion but not as much as for larger values of r_i, and then is depleted at a much slower rate than $n_{\rm n}$ for shell 3. Back diffusion replenishes the rapidly depleted neutron number density in shell 3 enough to make the graph for $n_{\rm n}$ actually increase, and $n_{\rm n}$ eventually reaches a homogeneous value, but at $T =$ around 0.08 GK, long after nucleosynthesis has played out.

Back in Figure (4.16) $n_{^4{\rm He}}$ for $r_i = 7.9 \times 10^5$ cm has a more pronounced spike at the boundary between the high and low density regions than $n_{^4{\rm He}}$ for $r_i = 10^5$, due to neutrons back diffusing into the high density region quickly enough to affect the final value of $n_{^4{\rm He}}$. But the innermost shells have large production of ^{4}He because nucleosynthesis occurs before diffusion there. So the final value of $n_{^4\mathrm{H}e}$ is larger than for smaller r_i in the innermost shells, and likewise in the outermost shells due to nucleosynthesis occuring there. Table (4.1) lists the overall mass fraction of ^{4}He at 0.229782, the lowest value $X_{^4\mathrm{He}}$ reaches for $\eta_{10} = 3.0$. For higher r_i, $X_{^4\mathrm{He}}$ now increases.

4.3.6 $r_i = 6.3 \times 10^6$ cm

For r_i higher than 7.9 $\times 10^5$ cm the nucleons in the high density shells and those in the low density shells act independently from each other. The high proton and neutron number densities in the inner shells lead to considerable production of ^{4}He, enough for $X_{^4\mathrm{He}}$ to start increasing again. Figure (4.21) show n_n, n_p and $4n_{^4\mathrm{He}}$ for $r_i = 6.3 \times 10^6$ cm. One can see in the figure n_n in the inner shells gradually decrease due to the neutron proton conversion reactions and then decrease steeply when nucleosynthesis occurs at around $T = 0.9$ GK. The final value in $n_{^4\mathrm{He}}$ in the shells is the uniform value that $n_{^4\mathrm{He}}$ started approaching in $r_i = 7.9 \times 10^5$ cm. In the outer shells n_n increases just a little bit right before nucleosynthesis occurs but nowhere near enough to reach the value of n_n in the inner shells.

Figure (4.22a) shows the neutron-proton conversion rates for shell 3 for this r_i, but no noticible diffusion from shell 3 to the outer shell 4 occurs before nucleosynthesis. Figure (4.22b) shows back diffusion from shell 4 back to shell 3 and that diffusion eventually equalizes n_n in all the shells. But this back diffusion becomes significant only when $T =$ around 0.06 GK. Diffusion of neutrons into shell 62 does not occur until $T = 1.0$ GK, as shown in Figure (4.23a). The diffusion makes the n $\rightarrow$ p reaction rate go up slightly. But then

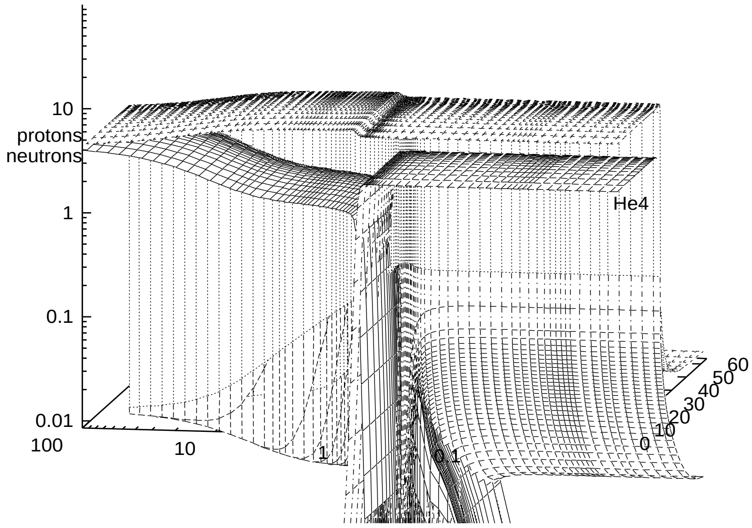

Figure 4.21: $n_{\rm n}$, $n_{\rm p}$ and $4n_{^4{\rm He}}$ for $r_i = 6.3 \times 10^6$ cm. $n_{\rm n}$ reaches a homogeneous value at around $T = 2.0$ GK.

the rate falls due to nucleosynthesis. Figure (4.23b) shows that back diffusion takes over when $T = 0.5$ GK. The overall mass fraction of ^{4}He is 0.250711 for $r_i = 6.3 \times 10^6$ cm, and $X_{^4{\rm He}}$ continues to increase with increasing r_i reaching a value that one would get by averaging the results of a standard BBN code with a high baryon density with the results of a standard code with a low baryon density.

4.3.7 Summary of Results

Figures (4.16) and (4.20) review the results calculated when one varies r_i along a set $\eta_{10} = 3.0$. Figure (4.20) shows $n_{\rm n}$ as a function of temperature for shells 3 and 62, and Figure (4.16) shows the final value of $4n_{^4{\rm He}}$ in all the shells. In

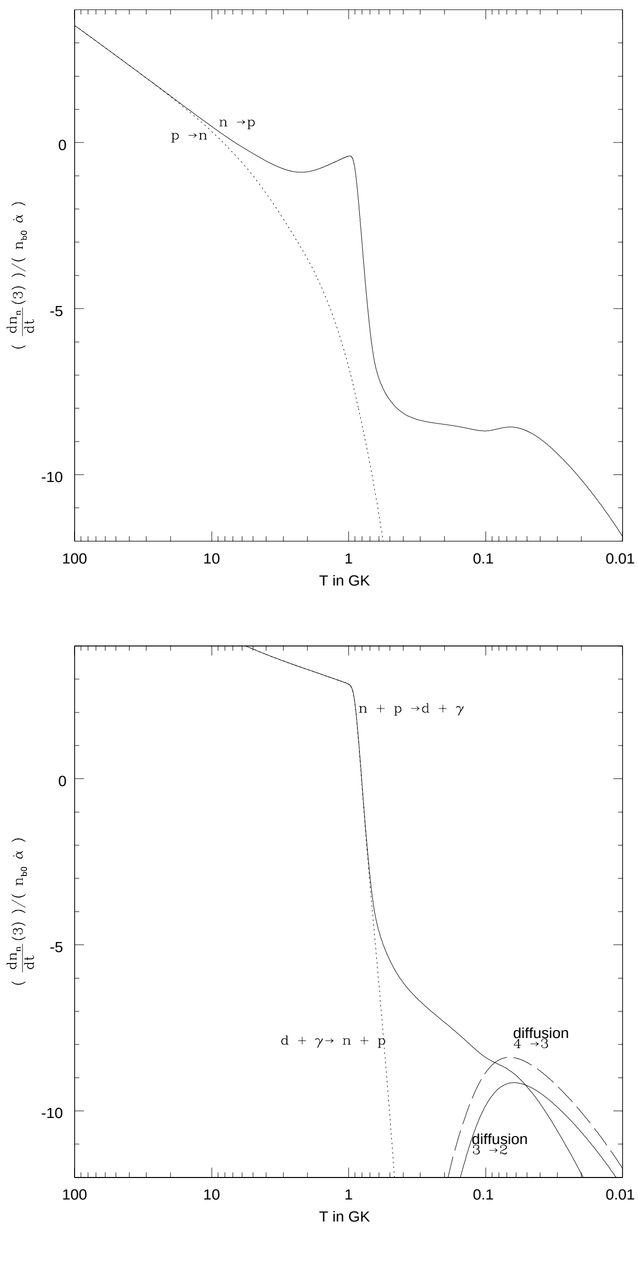

Figure 4.22: The neutron-proton conversion rates in shell 3 (4.22a), and the back diffusion rates compared with the nuclear reaction rate n + p $\leftrightarrow$ d + γ (4.22b). Here $r_i = 6.3 \times 10^6$ cm. No noticible diffusion happens in the temperature range of (4.22a).

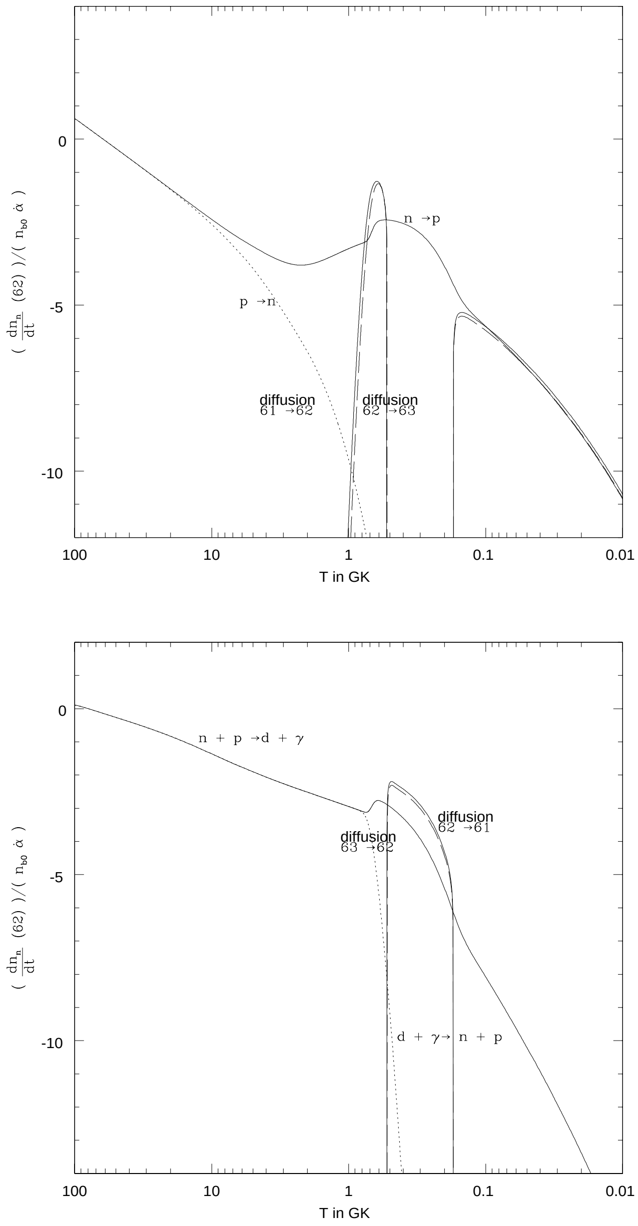

Figure 4.23: The neutron diffusion rates into and out of shell 62 compared with the neutron-proton conversion rates in shell 62 (4.23a), and the back diffusion rates compared with the nuclear reaction rate n + p $\leftrightarrow$ d + γ (4.23b). Here $r_i = 6.3 \times 10^6$ cm.

Figure (4.20) one can see the values of n_{n} converging into one value for the first four values of r_i. After nucleosynthesis the graphs spread out somewhat, depending on the difference in total baryon density between the shells. For the last two values nucleosynthesis occurs before diffusion can homogenize the neutrons. n_{n} for shell 3 plummets while n_{n} for shell 62 increases at first due to neutrons coming in but then undergoes nucleosynthesis before it can reach a homogeneous value. These graphs for n_{n} do not come to a common value until considerably sometime after nucleosynthesis. In Figure (4.16) one sees again how $n_{^4\mathrm{He}}$ has the same value in all shells for the lowest r_i, 100 cm. Then $n_{^4\mathrm{He}}$ has a somewhat higher value in the inner shells than the outer shells for $r_i =$ 1600 cm, because of the larger amount of protons left in the inner shells. At $r_i = 25000$ cm $n_{^4\mathrm{He}}$ reaches a maximum value in the inner shells as the inner shells now retain nearly all their protons and back diffusion is quick enough to move all neutrons into the inner shells during nucleosynthesis. At $r_i = 10^5$ cm back diffusion does not occur not quickly enough for neutrons to reach all the inner shells, and so ^{4}He is produced more in the shells near the boundary. A spike in the graph of $n_{^4\mathrm{He}}$ arises around the boundary when $r_i = 7.9 \times 10^5$ cm, but here nucleosynthesis occurs in the innermost shells before diffusion can deplete the neutrons, and so $n_{^4\mathrm{He}}$ has a larger value in the innermost shells. Finally at $r_i = 6.3 \times 10^6$ cm $n_{^4\mathrm{He}}$ reaches a plateau value in the inner shells as nucleosynthesis dominates the results in those shells. The plateau coincides with the plateau for $r_i = 25000$ cm as in both cases the overwhelming amount of neutrons in the whole model are worked into the nucleosynthesis process in the inner shells.

4.4 The Neutrino Heating Effect in an Inhomogeneous Model

Electrons, positrons, and neutrinos are distributed homgeneously in this code. The diffusion coefficient for neutron-electron scattering, Equation (4.2), depends on n_{e}. The terms in (4.2) that depend on $z = m_{\mathrm{e}}/kT$ are determined from an integral built on the distribution functions of neutrons and electrons [48]. The Texas IBBN code has sections calculating the neutrino heating effect during a run. These sections solve for the neutrino distribution functions and use the distribution functions to calculate the neutrino energy and number densities and the temperature T of the electromagnetic plasma. The code does not change the Fermi-Dirac distribution functions of the electrons and positrons. The effect on the electrons and positrons is accounted for via the change in T. Therefore, Equation (4.2) does not need to be modified in order to be consistent with the neutrino heating sections of the code. D_{ne} will change due to the decrease of n_{e}, and the Bessel functions

$$\begin{aligned} K_2(z) &= \frac{1}{z^2}\int_0^\infty dk k^2 e^{-\sqrt{k^2+z^2}} \\ K_{5/2}(z) &= \sqrt{\frac{\pi}{2}}\frac{1+\frac{3}{z}+\frac{3}{z^2}}{e^z\sqrt{z}} \end{aligned}$$

change due to the change in the value of T.

4.4.1 The change of $X_{^4\mathrm{He}}$

Figure (4.24) shows $10^4 \times \Delta X_{^4\mathrm{He}}$ as a function of η and r_i. In the standard code $\Delta X_{^4\mathrm{He}}$ has a range from 2.0×10^{-4} down to 1.1×10^{-4} for the range of η shown in

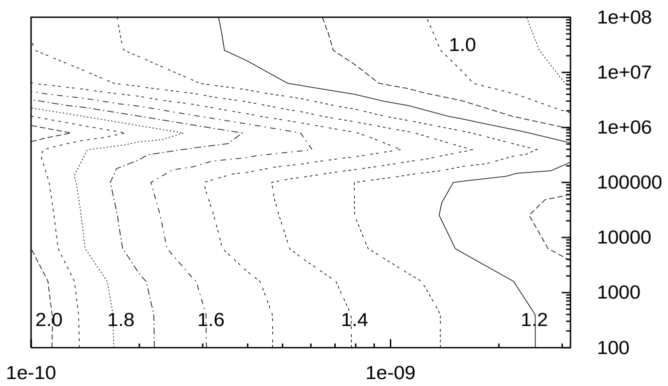

Figure 4.24: $10^4 \times \Delta X_{^4\mathrm{He}}$ in the IBBN code due to neutrino heating. $\Delta X_{^4\mathrm{He}}$ remains in the order of magnitude of 10^{-4} and this figure roughly tracks (4.2b), the graph for $X_{^4\mathrm{He}}$.

(4.24), and decreases with increasing value of $X_{^4\mathrm{He}}$. The inhomogeneous code reflects these results in the graph for $r_i = 100$ cm and somewhat higher. For the whole range of r_i $\Delta X_{^4\mathrm{He}}$ stays within the order of magnitude of 10^{-4}. The contour lines of (4.24) roughly mimic the contour lines of $X_{^4\mathrm{He}}$ in Figure (4.2b) with $\Delta X_{^4\mathrm{He}}$ decreasing when $X_{^4\mathrm{He}}$ increases. The neutrino heating effect on ^{4}He is comparable to the effect of a slight increase in η, with the increase ranging from 1 % to 2 %.

Figures (4.25) to (4.28) correspond to the case of $\eta = 3 \times 10^{-10}$ and $r_i =$ 25000 cm. For those parameters the protons in the innermost shells do not get redistributed and back diffusion sends nearly all neutrons to the inner shells for nucleosynthesis, and $X_{^4\mathrm{He}}$ starts decreasing. Figure (4.25a) shows the rates

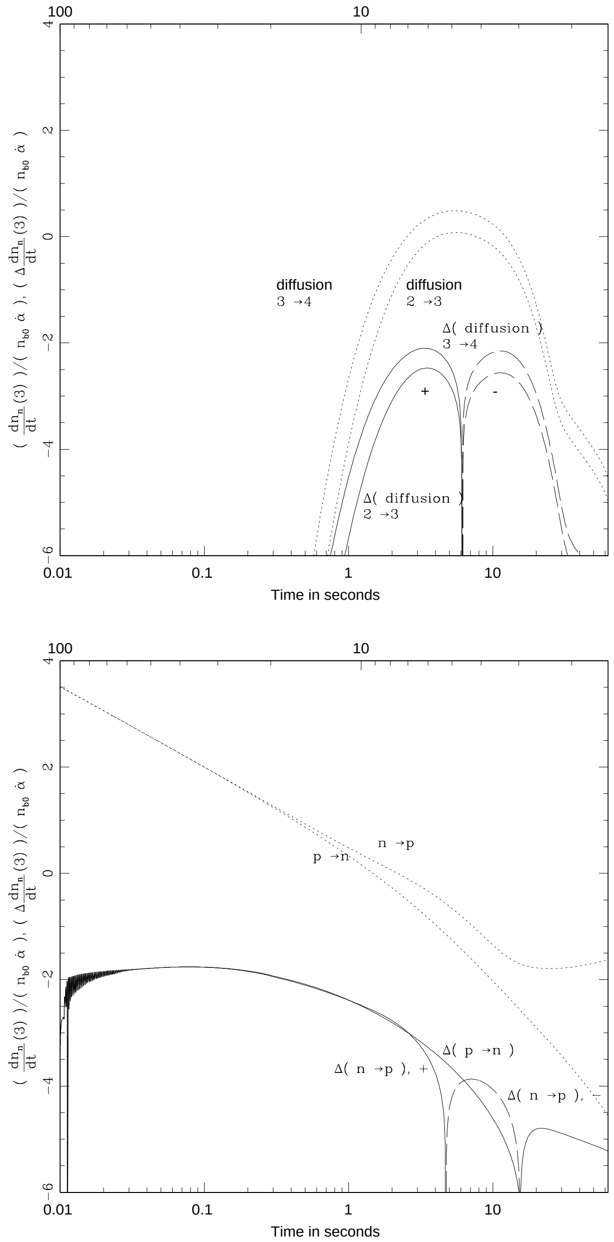

Figure 4.25: Shell 3, $r_i = 25000$ cm, and $\eta_{10} = 3.0$. Neutrino heating shifts the diffusion rates slightly earlier (4.25a). Heating has the same effect on the n-p conversion rates in the IBBN code as it does in the standard code (4.25b).

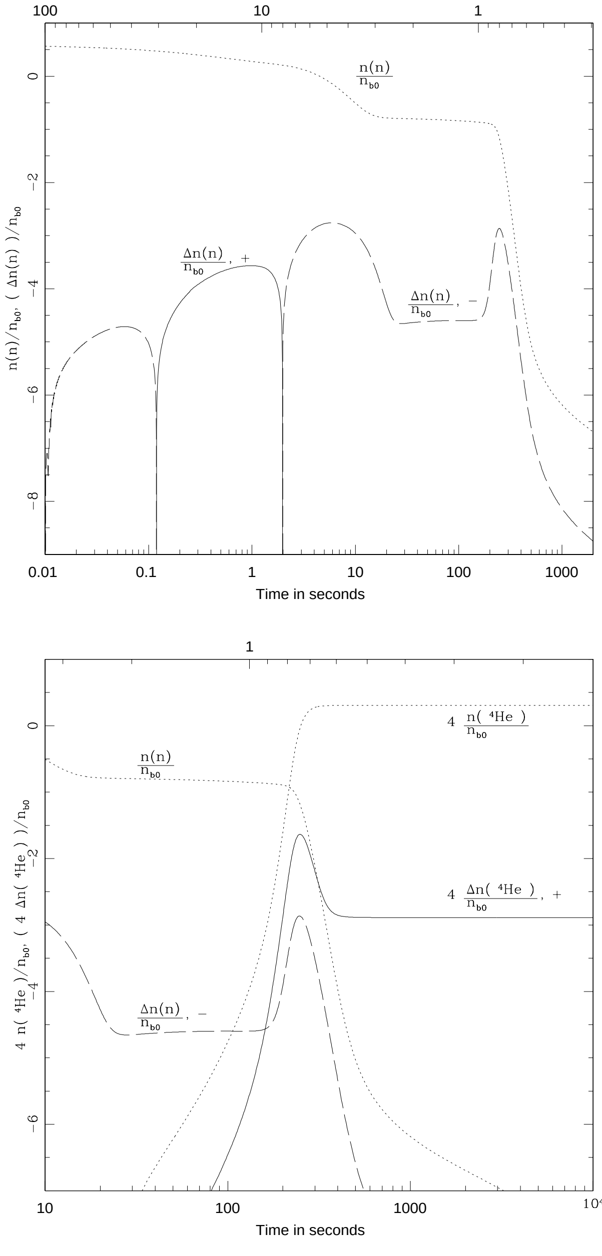

Figure 4.26: Δn_{n} (4.26a) and $4\Delta n_{^4\mathrm{He}}$ (4.26b) due to neutrino heating in shell 3 for $r_i = 25000$ cm, and $\eta_{10} = 3.0$. The results are similar to the results in the standard code.

of diffusion from shell 2 into shell 3 and from shell 3 out to shell 4 with the heating effect turned on. The graph also shows the change in the diffusion rates due to the effect. The graphs are shown as functions of time instead of temperature as the effect changes the temperature. For both rates the change is positive up to time $t = 6.0$ seconds, and then the change turns negative. These results means that the diffusion rates are shifted to an earlier time. At any certain time the heating effect decreases T, and a decrease in T means D_{ne} has a value that it would have at a slightly later time. The shift in time is around 0.1 %. Figure (4.25a) is for diffusion before nucleosynthesis, but the back diffusion rates during nucleosynthesis have the same leftward shift. So the neutrino heating effect makes diffusion occur earlier, but it has a far less effect on diffusion than the value of r_i does.

Figure (4.25b) shows the neutron-proton conversion rates for shell 3, and the change in the rates due to neutrino heating. The rates are different from the rates shown in Chapter 3's figures such as (3.5a) and (3.5b) in that they are $\lambda(\mathrm{n} \leftrightarrow \mathrm{p})$ times $n(3, \mathrm{n})$ or $n(3, \mathrm{p})$. The graphs correspond to $dn(3, \mathrm{n})/dt$, but they still have the same shape as the graphs for $\lambda(\mathrm{n} \leftrightarrow \mathrm{p})$ alone in Figures (3.5a) and (3.5b). As in those figures the changes due to the heating effect are increases for both $\mathrm{n} \rightarrow \mathrm{p}$ and $\mathrm{p} \rightarrow \mathrm{n}$ that nearly cancel each other out. But the heating effect makes diffusion occur slightly earlier and so neutrons are depleted slightly more quickly. This depletion causes the change in $\mathrm{n} \rightarrow \mathrm{p}$ to turn negative during diffusion. But the change becomes positive again once the neutrons are homogeneously distributed.

Figure (4.26a) shows that the heating effect changes the neutron number density $n(\mathrm{n})$ in shell 3 similarly to how it changes the mass fraction X_{n} in the standard code in Figure (3.5c). The conversion rates are closer in equilibrium at the higher temperatures. Δn(n) becomes positive at slightly more than 0.1 second, the same as in the standard case. Figure (4.25b) shows that the change in the p $\rightarrow$ n rates is slightly larger than the change for n $\rightarrow$ p rates for the time period when Δn(n) is positive. When diffusion occurs neutrons deplete rapidly, and Δn(n) becomes negative at a time of 2.0 seconds, earlier than in the standard code. As in the standard case the heating effect causes nucleosynthesis to occur earlier in shell 3, leading to the peak in the graph for Δn(n) right before the graph falls along with n(n) itself.

Figure (4.26b) shows the change in the number density $n(^4\mathrm{He})$ as well as that for n(n). The behavior is the same as shown for the standard code in Figure (3.5d). $n(^4\mathrm{He})$ and $\Delta n(^4\mathrm{He})$ are multiplied by four so that the graphs will be comparable to the graphs for $X_{^4\mathrm{He}}$ and $\Delta X_{^4\mathrm{He}}$ in Figure (3.5d). The heating effect makes nucleosynthesis occur earlier and the graph for $n(^4\mathrm{He})$ flattens out earlier and higher than the graph without heating, leading to the peak shape of $\Delta X_{^4\mathrm{He}}$.

Figures (4.27) and (4.28) show the same values as shown in Figures (4.25) and (4.26) for the outer shell 62. The diffusion rates in (4.27a) have the same leftward shift as the rates in (4.25a) have. The changes in the conversion rates in (4.27b) are similar to the changes in (4.25b) but three orders of magnitude smaller, reflecting the low neutron number density in the outer shell. But diffusion brings in neutrons in a large quantity, and so the change in the n $\rightarrow$ p rate has a large increase along with the n $\rightarrow$ p rate itself.

In Figure (4.28a) Δn(n) changes from negative to positive at later than 0.1 second, same as for shell 3. But diffusion brings in a large increase in neutrons to shell 62, so Δn(n) remains positive for a longer time, up to $t =$ 20.0 seconds. When Δn(n) does turn negative it has the same value in shell 62

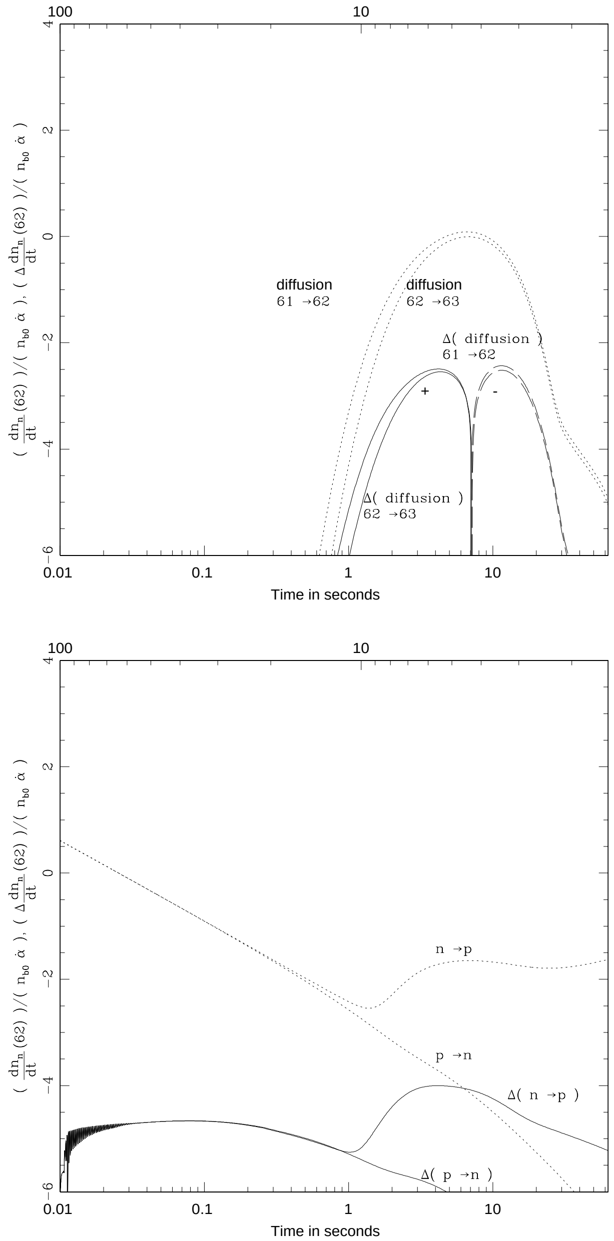

Figure 4.27: Shell 62, $r_i = 25000$ cm, and $\eta_{10} = 3.0$. Neutrino heating shifts the diffusion rates slightly earlier (4.27a). Heating has the same effect on the n-p conversion rates in the IBBN code as it does in the standard code (4.27b).

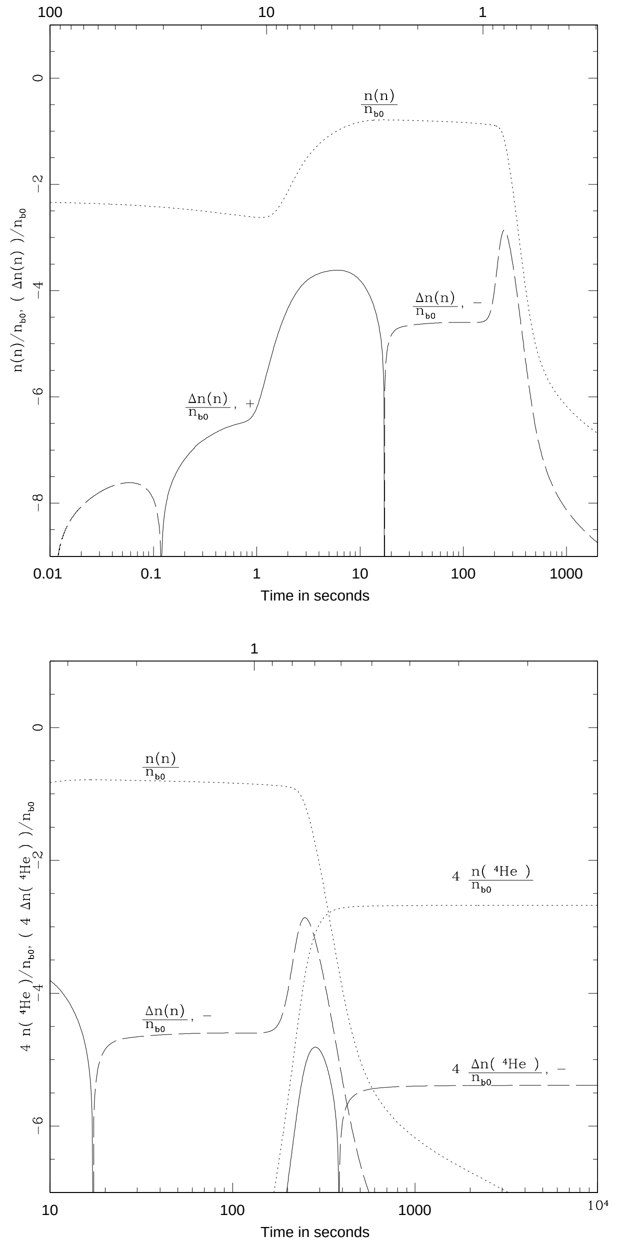

Figure 4.28: Δn_{n} (4.28a) and $4\Delta n_{^4\mathrm{He}}$ (4.28b) due to neutrino heating in shell 62 for $r_i = 25000$ cm, and $\eta_{10} = 3.0$. The rapid depletion of neutrons due to back diffusion leads to a negative value for $4\Delta n_{^4\mathrm{He}}$.

as in shell 3, reflecting the homogeneous distribution of the neutrons. Shell 62 still has much fewer protons than shell 3, though. The graphs for $n(^4\mathrm{He})$ and $\Delta n(^4\mathrm{He})$ are then small for shell 62. Further, back diffusion sends neutrons back to the inner shells rather than have them undergo nucleosynthesis in the outer shells. So $\Delta n(^4\mathrm{He})$ ultimately winds up negative. Only the outermost shells have a negative change in $n(^4\mathrm{He})$, though. The overall neutrino heating effect is to increase the mass fraction $X_{^4\mathrm{He}}$ from 0.243686 to 0.243838, a difference of 1.52×10^{-4}

The production of nuclei is influenced by the behavior of electrons, positrons and neutrinos rather than the other way around. The electron number density n_e and the electromagnetic plasma temperature T is the same for all shells in the inhomogeneous code. So the change in the diffusion coefficient D_ne for neutron/electron scattering is uniform over all the regions, and the baryon inhomogeneity has no influence on the transfer of energy between neutrinos and electrons/positrons. Since the changes in T and n_e are small the change in the diffusion rates is small, a leftward shift making diffusion earlier. So the increase in ^{4}He remains within the order of magnitude of 10^{-4} throughout the range of η and r_i that this author observes, increasing in magnitude when $X_{^4\mathrm{He}}$ decreases.

4.4.2 The change of $Y(\mathrm{d})/Y(\mathrm{p})$

Figure (4.2a) shows a contour map of $\log[Y(\mathrm{d})/Y(\mathrm{p})]$. For r_i low enough for the neutrons to homogenize before nucleosynthesis Figure (4.2a) roughly tracks Figure (4.2b), the contour map of $X_{^4\mathrm{He}}$. But for r_i large enough that diffusion can't occur before nucleosynthesis both $\log[Y(\mathrm{d})/Y(\mathrm{p})]$ and $X_{^4\mathrm{He}}$

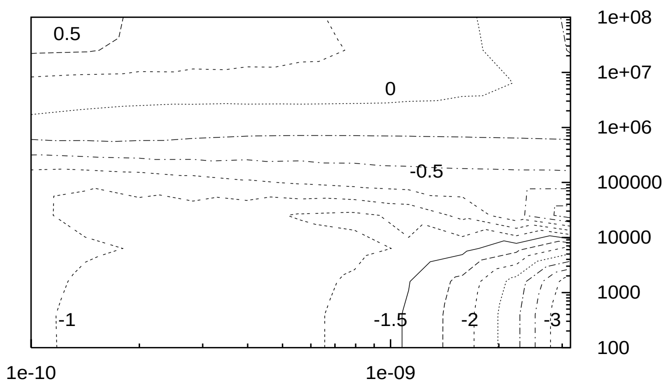

Figure 4.29: $10^3 \times \Delta(\log(Y(\mathrm{d})/Y(\mathrm{p})))$ in the IBBN code due to neutrino heating. The change goes from negative to positive when $r(i)$ is too great for neutron diffusion to occur before nucleosynthesis.

have large values in comparison to their standard model values. Figure (4.29) shows $10^3 \times \Delta\{\log[Y(\mathrm{d})/Y(\mathrm{p})]\}$, the change in the amount of deuterium due to the neutrino heating effect. For $\eta_{10} = 3.0$ and $r_i =$ around 25000 cm $\log[Y(\mathrm{d})/Y(\mathrm{p})]$ decreases by only 1.12 $\times 10^{-3}$ (X_{d} goes from 0.834930 $\times 10^{-4}$ down to 0.832613 $\times 10^{-4}$.). This author compares the neutrino heating results with the results that come from changing the value of η. If one increases η by 1.53 %, to 3.046 $\times 10^{-10}$ the mass fraction $X_{^4\mathrm{He}}$ increases to the same value as it does due to neutrino heating. But $\log[Y(\mathrm{d})/Y(\mathrm{p})]$ decreases by 9.19 $\times 10^{-3}$, nearly an order of magnitude more than the case with neutrino heating (X_{d} falls from 0.834930 $\times 10^{-4}$ down to 0.817291 $\times 10^{-4}$.).

Figure (4.30) shows for shell 3 the rate for the nuclear reaction n + p

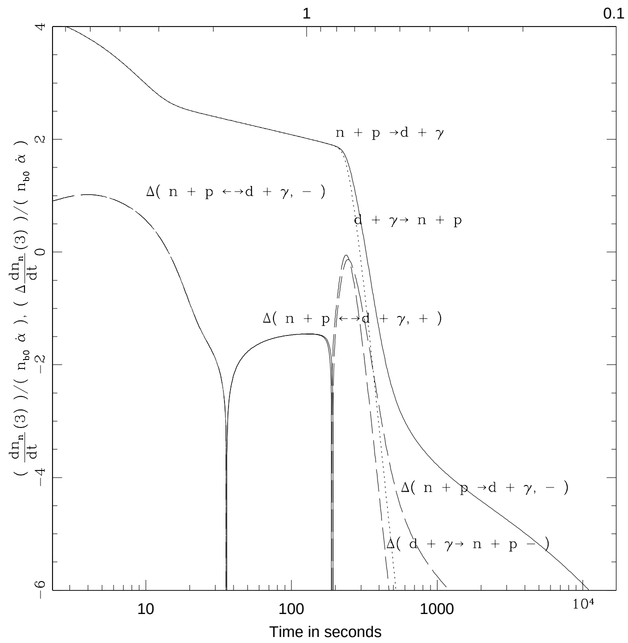

Figure 4.30: Neutrino heating decreases temperature T and causes neutron diffusion and nucleosynthesis to occur earlier. These effects change the rate for the reaction n + p $\leftrightarrow$ d + γ

$\leftrightarrow$ d + γ and the change $\Delta(\mathrm{n} + \mathrm{p} \leftrightarrow \mathrm{d} + \gamma)$ of the foward direction rate and the reverse direction rate due to neutrino heating. Neutrino heating lowers the temperature T at a given time because of the electrons and positrons losing energy. In shell j these reaction rates obeys the equation [15]:

$$\begin{aligned} [\mathrm{np}](j) &= \rho_b(j)\frac{4.17 \times 10^8}{T_9^{2/3}}(1.0 + 0.098T_9^{1/3} + 0.518T_9^{2/3} \\ &\quad +0.355T_9 - 0.01T_9^{4/3} - 0.018T_9^{5/3})e^{-4.258/T_9^{1/3}} \\ (\mathrm{d}\gamma)(j) &= (0.472 \times 10^{10})T_9^{3/2}[\mathrm{np}](j)/\rho_b(j)e^{-25.816/T_9} \end{aligned}$$

where $T_9 = 10^{-9}T$. The reaction rates at first are shifted to slightly earlier times, This shift is indicated by the negative values of $\Delta(\mathrm{n} + \mathrm{p} \leftrightarrow \mathrm{d} + \gamma)$

for both directions, negative because the rates are decreasing functions of time/temperature. (Due to NSE though the decreases are equal for both directions.) Neutrino heating causes neutron diffusion to occur earlier. At a given time after diffusion then shell 3 will have fewer neutrons and hence a lower $\rho_b(3)$. After diffusion n + p $\leftrightarrow$ d + γ then has a flatter slope than without heating. The rates become greater for the case with heating, and $\Delta(\mathrm{n+p} \leftrightarrow \mathrm{d}+\gamma)$ in Figure (4.30) has a brief period with a positive magnitude. The flatter slope also makes $\Delta(\mathrm{n+p} \leftrightarrow \mathrm{d}+\gamma)$ increase in magnitude over time during the time that it has a positive magnitude. The increase is still equal for both directions, though. Finally nucleosynthesis occurs earlier because of heating. The reaction rates plummet earlier and $\Delta(\mathrm{n} + \mathrm{p} \leftrightarrow \mathrm{d} + \gamma)$ for both directions become negative again, with peaks as indicators of the clock effect. Also, it's only when the directions fall out of equilibrium when $\Delta(\mathrm{n+p} \leftarrow \mathrm{d}+\gamma)$ diverges from $\Delta(\mathrm{d} + \gamma \leftarrow \mathrm{n} + \mathrm{p})$. Changing the rates by changing T seems to have a much smaller effect then by changing ρ_b.

Figure (4.31) shows the rates n + p $\leftrightarrow$ d + γ and the changes $\Delta(\mathrm{n+p} \leftrightarrow \mathrm{d}+\gamma)$ for shell 62. The reaction rates become increasing functions of time when neutrons diffuse into shell 62. Earlier diffusion due to neutrino heating causes $\rho_b(62)$ to increase from the value it has without heating. So the rates have steeper slopes after diffusions. In Figure (4.31) neutrino heating increases the reaction rates for a longer period of time for shell 62 than shell 3. The steeper slope leads to $\Delta(\mathrm{n+p} \leftrightarrow \mathrm{d}+\gamma)$ decreasing in magnitude in the time when it has a positive magnitude. $\Delta(\mathrm{n+p} \leftrightarrow \mathrm{d}+\gamma)$ become negative when nucleosynthesis occurs earlier due to neutrino heating.

For $r(i) > 7.9 \times 10^5$ cm the high density inner shells and the low density outer shells behave independently. Baryon-to-photon ratios lower than $\eta =$

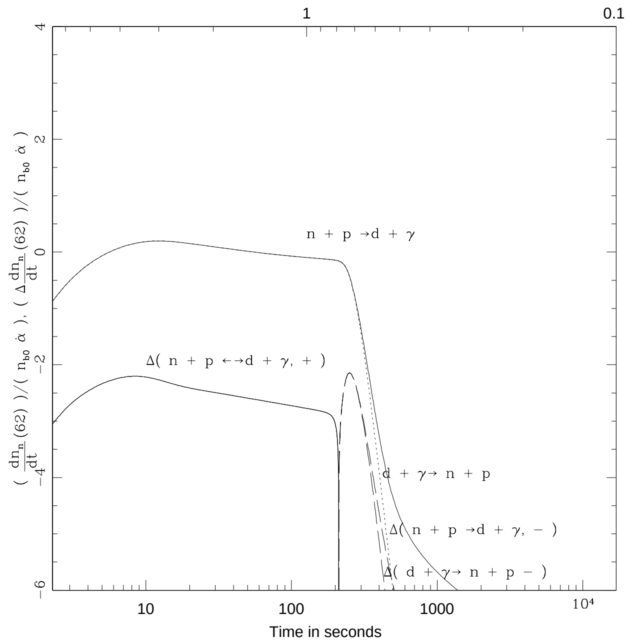

Figure 4.31: Neutrino heating changes the rate for n + p $\leftrightarrow$ d + γ in shell 62 in similar manners as heating does in shell 3.

10^{-10} produce much more deuterium. Ratios higher than $\eta = 10^{-9}$ produce more ^{4}He. So $X_{^4\mathrm{He}}$ and $Y(\mathrm{d})/Y(\mathrm{p})$ have values larger than their homogeneous values for $r(i)$ in this range. Figure (4.29) also reveals that the increased production of deuterium in the low density shells causes deuterium to increase due to neutrino heating for large $r(i)$, instead of decrease.